2023-08-01

Holocene variations in the Asian Summer and Winter Monsoons reconstructed from extensive lacustrine sediments in the Mu Us Desert, northern China

Wen, X

https://pearl.plymouth.ac.uk/handle/10026.1/20939

Holocene variations in the Asian Summer and Winter Monsoons reconstructed from extensive lacustrine sediments in the Mu Us Desert, northern China

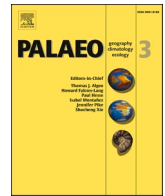Xiaohao Wen [a], Matt W. Telfer [b,*], Baosheng Li [a], Wei Wang [a], Tim Daley [b], Chen Wang [c], Mengyuan Tian [a], Mingkun Qiu [a]

[a] School of Geographical Science, South China Normal University, Guangzhou 510631, PR China
[b] School of Geography, Earth and Environmental Sciences, Plymouth University, Drake Circus, Plymouth, Devon PL4 8AA, UK
[c] School of Science, Tibet University, Lhasa 850000, PR China

ARTICLE INFO

ABSTRACT

The Salawusu River Valley cuts through the Mu Us Desert in north central China, and lies at the interface of the East Asian Summer and Winter Monsoonal regions. Exposed at numerous locations in the valley side are extensive late Quaternary deposits, consisting of interbedded aeolian sands, fluvio-lacustrine units and palaeosols. Due to the importance of the location in potentially elucidating both summer and winter monsoonal regimes, and the quality of the sedimentary record, the region has a rich history of study, and yet even within the Holocene sequence, many conflicting interpretations have arisen based on studies on different sections. This paper aims to synthesize and explore these differences by exploring the lateral continuity of the Holocene sequences along a ∼ 45 km reach of the valley, and presenting new, detailed physical and geochemical analyses of three sections, focusing on the lacustrine Holocene Dagouwan Formation.

The absence of the lacustrine unit at several locations confirms that rather than representing a single lake, the Dagouwan Formation instead represents a series of palaeolakes, probably at least partially hydrologically isolated from each other by aeolian sands. All begin with sand-dominated deposits during the early−/mid-Holocene, which is interpreted as the result of abundant sand-supply to the north and west, under the influence of an enhanced East Asian Winter Monsoon, and all switch to silt-dominated, more carbonate-rich deposits during the mid−/late-Holocene, which is attributed to an enhanced East Asian Summer Monsoon bringing loessic silts from the Chinese Loess Plateau to the east and south. The timing of this change, perhaps as late as 5.5 ka, supports the idea of a relatively enhancement late mid-Holocene of the summer monsoonal circulation in the region.

However, despite the proximity of the sections and consistent analytical approaches, marked differences between the sections occur in all proxies studied. The timing and rate of the switch from sand- to silt-dominated lacustrine deposition varies between the sites by as much as 2000 years within just a few kilometres of each other, and at some sites the switch was gradual, whereas at others it was very rapid. Similar dramatic variations are also seen with organic carbon content, carbonate content, C:N ratio, and especially the $\delta^{13}C$ isotopic ratio. These point to the lake basins behaving very differently, and emphasize that consideration must be given to the local geomorphology and palaeolimnological evolution of individual sections.

1. Introduction

1.1. Holocene dynamics of the East Asian Monsoons

The climate and weather of East Asia are dominated by the East Asian Monsoon (EAM) systems, which consist of the East Asian Summer Monsoon (EASM), which brings warm, moist air from the Pacific to continental Asia, and the East Asian Winter Monsoon (EAWM), which brings cold, dry air from the interior of the continent to its margins. Their phase relationship between the two systems is complex, and has varied over time (Kaboth-Bahr et al., 2021; Lu et al., 2022), and is further complicated by interactions with the Indian Summer monsoon

(ISM) (Ding and Chan, 2005) and teleconnections with the Pacific (Wang, Wu & Fu, 2000) and Atlantic (Sun and Wang, 2012; Wu et al., 2012).

The importance of the EAM systems is hard to overstate; estimates vary widely, but even at the most conservative range of the scale, at least 20% of the world's population relies on the EASM for water (e.g. Shi et al., 2021). Throughout numerous glacial cycles, the EAWM has been responsible for the transport and deposition of vast quantities of dust, resulting in the accumulation of the Chinese Loess Plateau (CLP), the largest accumulation of loess in the world (Sun, 2002). In modern times, the intensity of the EAWM has been associated with decadal-scale variation in the presence of dust weather events the Chinese capital, Beijing (Wu et al., 2010). The monsoons' impact stretches beyond the immediate region, and they impact global hydrological and dust cycles. The EAM systems have varied in strength and position throughout the Quaternary (An et al., 2000), and may do so under the impact of present-day anthropogenic climate change (Burke and Stott, 2017; Jiang and Tian, 2013). Understanding the spatiotemporal sensitivity of the EAM to past changes in global forcing in the past is thus of great importance. A wide range of proxies and archives have been exploited to help understand past changes, including the sedimentology of the loess record (e.g. An et al., 2001; Xiao et al., 1995; Wang et al., 2014), speleothem isotope records (e.g. Wang et al., 2001; Wang et al., 2008; Zhang et al., 2021), lacustrine records (e.g. Chen et al., 2015) and ocean core records of the adjacent seas (e.g. Wang et al., 1999; Zhang et al., 2019). However, the interpretation and synthesis of many of these proxies has proven difficult, with the speleothem isotope records especially challenging to interpret palaeoclimatically (Clemens et al., 2010; Liu et al., 2014b). To this end, new records and coherent syntheses of the monsoon dynamics of East Asia are especially valuable.

1.2. Terrestrial records of the EAM at the margins of the Mu Us Desert and Chinese Loess Plateau

The Salawusu (sometimes transliterated as Sarawusu, Sala Us or Sara Us) River valley in Inner Mongolia, northern central China, lies in a region influenced by both the EASM and EAWM (Fig. 1). Interbedded sequences of aeolian and fluvial-lacustrine deposits are widely distributed and are potentially valuable terrestrial archives recording paleoclimate and paleo-environment throughout the Late Pleistocene (Li et al., 2000, 2007). Driven initially by Palaeolithic and archaeological studies (e.g. Licent et al., 1926), over the past century extensive studies have focused on the paleoenvironments and paleoclimate of the region and the implications for dynamics of the EASM and EAWM (e.g. Yuan, 1978; Li et al., 2000, 2007; Sun, 2000; Wen et al., 2009, 2021). Situated beyond the northern margin of the Chinese Loess Plateau (CLP), at the southern edge of the Mu Us Desert on the highland sedimentary basin of the Ordos Plateau (Fig. 1), the location of the Salawusu river valley offers an important location for sedimentological study, as aeolian sources – and thus the relative strength of the regional wind regime - can be readily inferred due to the distinct sedimentological characteristics of the adjoining regions. This is further facilitated by the rapid accumulation, varied sedimentology (interbedded lacustrine and aeolian sand units) and subsequent deep incision which has exposed the Dagouwan Formation (with a type-section at Dagouwan; DGW) (Li et al., 2000, 2007).

Numerous previous studies have confirmed the uppermost lacustrine deposits of the DGW to be of Holocene age, and paleo-hydrological and paleoclimatic changes have been discussed based on different dating methods and paleoclimatic proxies (e.g. Lu et al., 2010; Li et al., 2012; Liu and Lai, 2012; Zhao et al., 2016; Shu et al., 2016; Liu et al., 2018a), but these reconstructions have often proven inconsistent. Although sections such as Milanggouwan (MLGW) and Dishaogouwan (DSG) have been studied many times, sections have most commonly been studied individually, often with conflicting inferences, even over small spatial scales. For instance, at DSG, Zhao et al. (2016) inferred complicated

local environment changes during the Holocene and a humid period from 7.1 to 2.0 ka ago. Others have drawn very different conclusions from the same section; Liu and Lai (2012) interpreted grain-size data from the DSG section to reveal the wettest climatic conditions occurring during the early Holocene at around 11 ka and a subsequent climate showing a trend of increasing aridity (Liu and Lai, 2012). Conversely, dating results combined with environmental proxies from the DGW section, only about 2 km from DSG, implied that a dry environment existed in the early Holocene before 8.5 ka, followed by a wet environment (the "Holocene Climate Optimum" period) that took place from 8.5 to 5 ka BP, and that after 5 ka BP the region became arid, as inferred from lake regression (Li et al., 2002). Some results from different sites have concurred, with more recent studies of lithology and grain-size from DSG interpreted as an interval of relatively high lake-level from 8.4 to 4.0 ka BP, with a maximum lake level during 8.4 to 6.5 ka BP, which then gradually declined (Liu, 2018). Complicating these broadly hydrological interpretations have been those studies which instead have focused on thermal interpretations. Shu et al. (2016) interpreted grain size data at DSG to subdivide Holocene climate into four stages: the warming early Holocene (11,020 to 10,290 yr BP), Holocene altithermal (10,290 to 6590 yr BP), the fluctuation period from Megathermal to cold (6590 to 3760 yr BP), and cooling period of instability and desertification (3760 to 0 yr BP). Yet other studies, based on single sections yet using multiple proxies at the MGW section, indicated there existed 11 millennial-scale cold-dry and warm-humid climatic fluctuations during the Holocene Period (Li et al., 2000; Lu et al., 2010; Niu et al., 2008; Wang et al., 2021).

Possible reasons for these apparent contradictions and intricacies might include local differences in the catchments, different interpretations of different proxies at the sections, and the uncertainty in the chronologies (Liu and Lai, 2012; Zhao et al., 2016). Some have questioned whether individual selected sections can be considered regionally representative (Zhao et al., 2016), as the thickness of lacustrine deposits varies from place to place. Until now, the lateral spatial continuity of the lacustrine deposits of the Holocene sequence remains uncertain, and too often the potential geomorphological interconnectivity of the sequences has been ignored, and the sections considered only in isolation. Therefore, clarifying the spatial distribution of Dagouwan Formation lacustrine along the Salawusu River and synthesizing appropriate sedimentary archives is crucial for reconstructing robust regional constructions of the impact of the EASM and EAWM.

This study thus aims to: i) synthesize the stratigraphies of numerous sections of the Holocene Dagouwan Formation (both published and newly-investigated) to resolve depositional and chronological inconsistencies, ii) investigate the potential of geochemical and physical characteristics of the lacustrine component as a proxy for sediment source and thus monsoonal intensity and iii) investigate the consistency and synchroneity of lacustrine response, to dissociate localized geomorphological change from regional palaeoclimatic signals.

1.3. Study area

The Salawusu River valley (Fig. 1) lies mostly in the southeastern portion of Mu Us Desert and is a low relief transition zone between the southern part of the Ordos Plateau and the northwestern margin of Chinese Loess Plateau (CLP). The elevation varies from 1370 m above sea level in the southwest to 1000 m above sea level in the northeast. The ground surface is dominated by stabilized, semi-stabilized, and mobile dunes, of which the stabilized and semi-stabilized dunes consist of polygonal dunes, and the mobile dunes are composed of chains of crescentic dunes (Liu et al., 2014a). Steppes and interconnected sequences of shoals, marshes, and lakes are common in the relatively low-lying interdune areas.

The climate in the study area is characteristic of a warm-temperate semiarid continental monsoon environment, which is heavily
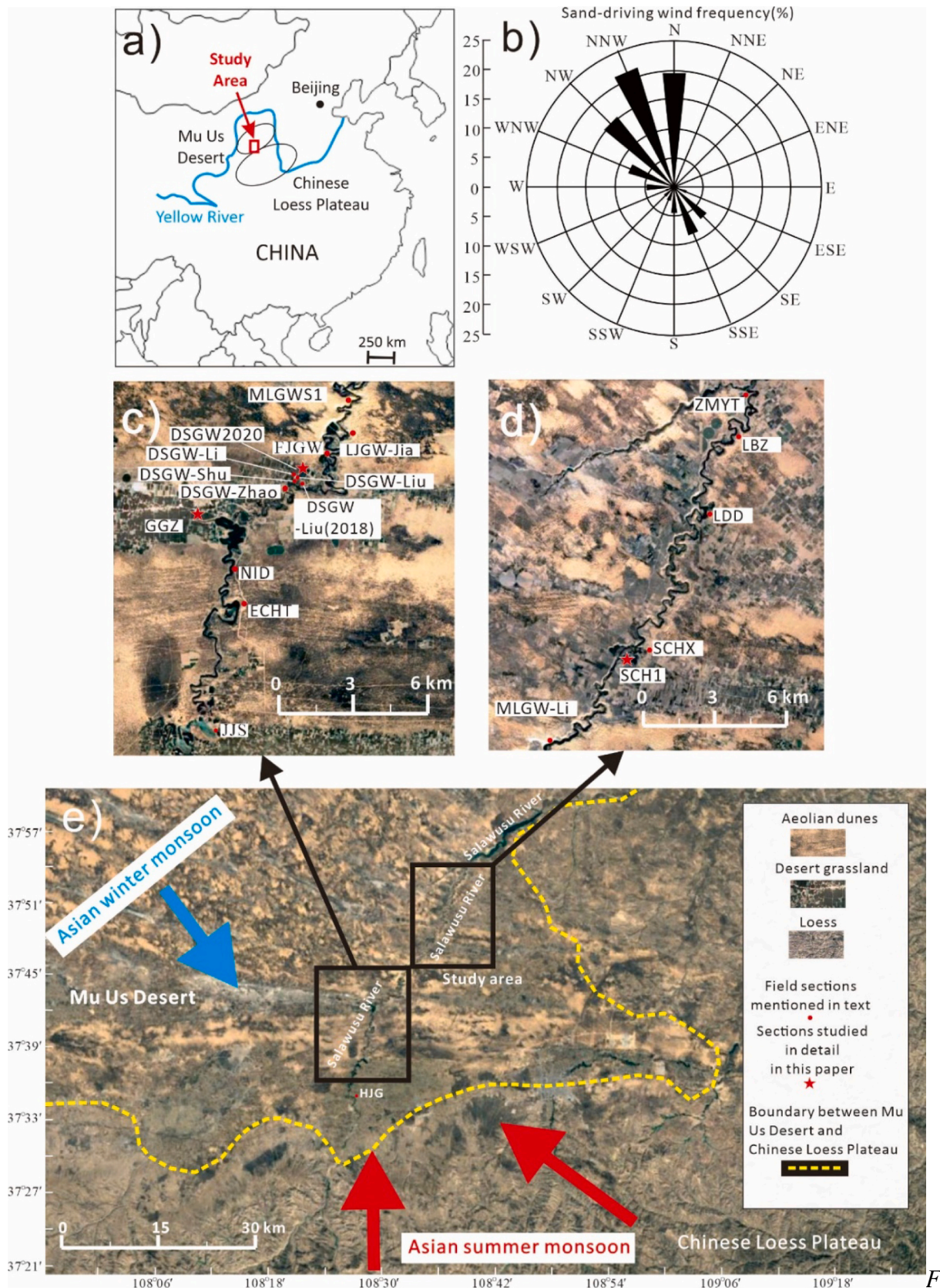
Fig. 1. a) Location of the study site within east Asia; b) Sand rose indicating the sand-driving wind frequency in Mu Us Desert (revised from Pang et al., 2019); c) and d) Detail of the study area with sampling sites, and those of sites reported in the literature; red stars represent the site of selected sections and red dots represent the sites of in-field investigated sections; e) The study area illustrating the context with the yellow dotted line representing the transition boundary between Chinese Loess Plateau and Mu Us Desert, and the dominant monsoonal winds indicated. (For interpretation of the references to colour in this figure legend, the reader is referred to the web version of this article.)

influenced and governed by the EAM systems. The EAWM, which transports northerly or northwesterly cold-dry continental air mass from Mongolia-Siberian high-pressure cell system, dominates the region in the winter and spring, with northerly or northwesterly winds dominating (Fig. 1) and brings frequent sand-dust storms. The EASM dominates this region in the summer and autumn, bringing the majority of the year's precipitation from the western Pacific Ocean and the Indian Ocean, with southerly or southeasterly winds prevailing (Fig. 1). The modern mean annual temperature ranges from 6 to 9 °C, and the mean annual rainfall is about 400 mm, ranging from 200 mm in the northwest to 450 mm in the southeast, with >60–70% falling between June and September, according to meteorological instrumental records of surrounding cities (such as Jingbian, Wushenqi, Dingbian, and others). However, rainfall is highly variable, ranging from 100 mm to 800 mm, with high-intensity rainstorms occurring sometimes, and yearly mean potential evaporation is 2500 mm (Wu et al., 2012). The average wind speed is 4.8 m/s, with a maximum of 20 m/s, and there are about 30 days of gale winds (>17 m/s) per year (Pang et al., 2019). The region's vegetation is characterized by shrubs (*Artemisia ordosica*, *Salix psammophila*, *Caragana korshinskii*) and annual to perennial plants (*Stipa capillata*, *Oxytropis campestris*, *Artemisia capillaris*, *Astragalus adsurgens*) (Zhang, 1994). Zonal soils, such as light chestnut soils, brown calcic soils, and nonzonal soils, such as black sandy loams, meadow soil, and saline-alkali soil, predominate.

2. Materials and methods

2.1. Investigations in the field

Extensive field investigations across the southeast section of the Mu Us desert and the neighbouring loess-mantled terrain of the northern CLP identified sections of the lacustrine deposits of the Dagouwan Formation (Li et al., 2000) (Fig. 3). These outcropped at the surface (Fig. 1, study area) and were tracked along both sides of the river reaches in the Salawusu River valley, over a straight distance of ~45 km from 37°35′N, 108°27′E to 37°58′N, 108°46′E. Pleistocene loess deposits and Cretaceous sandstone outcrops were also observed. Twenty outcrops of these lacustrine deposits were studied (Figs. 1 and 2), including eight outcrops (HJG, DSGW-Zhao, DSGW-Shu, DSGW-Li, DSGW-Liu, DSGW-Liu-2018, LJGW-Jia, and MLGW-Li) that have previously been described in the literature (Supplementary Material; Table S1). Twelve new sections (JJS, ECHT, NID, GGZ, DSGW2020, FJGW, MLGWS1, SCH, SCHX, LDD, LBZ, and ZMYT) are also reported in this study (Figs. 1 and 2). Sections were chosen to provide lateral sampling intervals of approximately every 2.5 km along the studied reach.

The lacustrine units of GGZ, DSGW2020 and SCH sections were chosen to be sampled for subsequent sedimentological examination due to the well-preserved characteristics and thickness of these outcrops. The locations of the three sections are shown on Fig. 1. Three samples of each selected section were picked from the top, middle, and bottom of each section to constrain the chronology with accelerator mass spectrometry (AMS) ^{14}C dates. For the grain size distribution, 125 samples for GGZ, 108 samples for DSGW2020, and 161 samples for SCH were sampled at 2 cm intervals. To evaluate the links between sensitive grain-
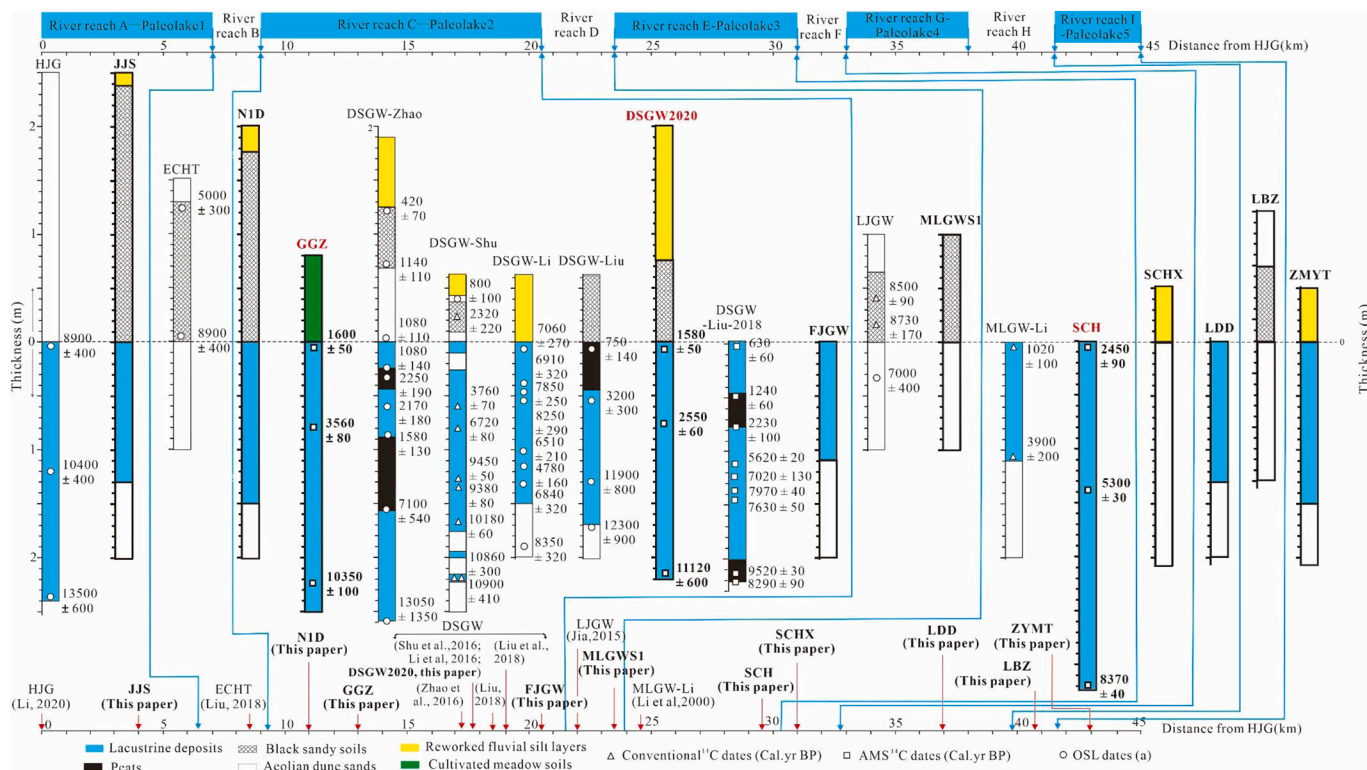

Fig. 2. Spatial distribution of Dagouwan Formation lacustrine deposits along a ~ 45 km section of the Salawusu river valley of the Mu Us Desert. This section of the Salawusu valley can be divided into nine reaches, depending on whether lacustrine deposits are present or not. Simplified stratigraphic profiles of twenty profiles of the Holocene sections are illustrated; nine from published literature (Li et al., 2000; Jia et al., 2015; Shu et al., 2016; Zhao et al., 2016; Liu et al., 2018; Liu et al., 2018a; Li, 2020), and eleven newly surveyed profiles (highlighted in bold). Of these eleven, three are analyzed in this study in more detail for geochemical and physical sedimentological properties (highlighted with red text). The elevation of all profiles is shown normalized to the top of the Dagouwan Formation lacustrine deposits, or the base of the overlying black soils and reworked fluvial deposits where lacustrine deposits are absent. Chronological controls, where available, are symbolized according to the methodology used; note substantial spatial variation in the onset and cessation of accumulation of the lacustrine unit. (For interpretation of the references to colour in this figure legend, the reader is referred to the web version of this article.)

size populations and dominant transport dynamics, samples of modern aeolian dune sands (20 samples), surface lacustrine sediments (8 samples), and Pleistocene loess deposits (11 samples) from the northern CLP were also collected for grain size measurements.

2.2. Experimental methods

2.2.1. Chronology

The nine accelerator mass spectrometry (AMS) ^{14}C dates on bulk organic matter from the GGZ, DSGW2020, and SCH sections were determined at the Beta Analytic Radiocarbon Dating Laboratory, using standard pretreatment procedures (Beta Analytic, 2022). The IntCal13 calibration curve given by version 8.1.0 of the Calib programme was used to calibrate all AMS ^{14}C dates to calendar years with a precision of ±2σ (Stuiver et al., 1998; Reimer et al., 2004, 2013). Table 1 contains detailed information. Many studies in the past have revealed very substantial reservoir effects with lacustrine sediments in northern, western and central China (Zhou et al., 2022). Based on analyses of five further AMS 14C assays, a reservoir correction of 530 years was determined (see Supplementary Material for full details of the methods, samples and results used to derive this number), which is consistent with recent reviews of the issue (Zhou et al., 2022).

2.2.2. Sediment analysis

To eliminate the organic matter and carbonates, approximately 0.5 to 1.0 g of each sample was placed in a 1000-mL beaker and boiled for 20 min with 30% hydrogen peroxide and adequate hydrochloric acid. To eliminate the dissolved cations, the beaker was then filled with deionized water. Finally, the solution in the beaker was ultrasonically dispersed with 10% sodium hexametaphosphate for several minutes before being left static overnight and the superstratum water was sucked away before the measurement. All pre-treated samples were analyzed to determine their grain-size distribution using a Mastersizer 2000 M laser diffraction instrument (Malvern Instruments, Malvern, U.K.), with a size detection range of 0.02–2000 μm, at the sediment analysis laboratory of the School of Geography, South China Normal University, Guangzhou, China.

Each sample was determined three times, with the average result being utilised in further analyses. The results of grain size were expressed as Φ, which is calculated as the negative log to the base 2 of the particle diameter in millimetres (Krumbein and Pettijohn, 1938). The mean diameter (Mz), standard deviation(σ), skewness (SK) and kurtosis (KG) were calculated using the equations proposed by Folk and Ward (1957).

Carbonate content was analyzed using a standard Bascomb calcimeter (Bascomb, 1961), with three to four analyses per sample to derive an average. Other geochemical analyses were conducted at the Huake Jingxin Stable Isotope Laboratory, Shenzhen City, China. All dried samples were ground using a porcelain mortar and pestle, and large particles and shoots or roots were removed by passing the samples through a 0.5 mm sieve. Bulk carbon and nitrogen content were determined using a Vario Macro Cube elemental analyzer. For isotopic

analyses, the sieved matter was treated by the acidification method to eliminate total inorganic carbon, and then isotopic analysis was accomplished by combustion in tin foil capsules and purification of CO_2. The carbon isotope (δ^{13}C) of the bulk organic materials were determined by an isotope ratio mass spectrometer (Finnigan Delta V Advantage, Thermo Fisher Scientific, Inc.). Results are expressed in delta (δ) notation relative to the V-PDB standard. Repeated analyses of lab standard carbonates with known δ^{13}C values were carried out to ensure instrumental accuracy. The analytical error of the laboratory standard is approximately ±0.1‰ for δ^{13}C, ± <0.5% for C%, ± <0.2‰ for δ^{15}N, ± <0.5% for N%.

3. Results

3.1. Spatial distribution of Dagouwan Formation lacustrine deposits along the Salawusu River valley

According to field surveys, horizontally the Dagouwan Formation lacustrine deposits stretch discontinuously over a straight-line distance of ~45 km along the Salawusu river valley, initiating at the Hejiagou (HJG) village, near Xinqiao reservoir, and terminating at Zhangmuyangtan (ZMYT) village, near Batuwan reservoir (Figs. 1 and 2). On the basis of the sedimentary sequence, it was separated into nine reaches (categorized as A - I). Layers of 1.3 to 2.4 m thick lacustrine deposits were observed in the 7 km long reach A, and they were buried by aeolian dune sands or black sandy soils. No Dagouwan Formation lacustrine deposits were found in the 2 km stretch B; instead, black sandy soils or aeolian dune sands were found. Five previously reported sections, here named DSGW-Li (Li et al., 2012), DSGW-Liu (Liu et al., 2012), DSGW-Zhao (Zhao et al., 2016), DSGW-Shu (Shu et al., 2016), and DSGW-Liu-2018 (Liu et al., 2018a), as well as three new explored sections, designated NID, GGZ, and DSGW2020, were used to represent the 11.5 km of reach C. Here, the Dagouwan Formation lacustrine deposits were widely distributed and covered by aeolian dune sands, black sandy soils, or fluvial layers. The thickness of the lacustrine deposits was variable, and ranged from 1 to 2.5 m. In the fourth reach (D), no lacustrine deposits are found within the Dagouwan Formation; instead, aeolian dune sands and black sandy soils were deposited, with the latter yielding reported ages of 8500 ± 90 cal yr BP and 8730 ± 170 cal yr BP (Jia et al., 2015). The alternating pattern of outcropping of the lacustrine deposits continues downstream, with the 2 km-long reach F and 3.5 km-long reach H yielding no lacustrine deposits, but aeolian dune sands, black sandy soils, and reworked fluvial layers. Conversely, layers of lacustrine deposits between 1.1 m and 3.2 m characterized the 7.5 km of reach E, and a 1.3 m lacustrine deposit outcropped in the 5 km of reach G. In both of these reaches, the lacustrine sediments outcropped at or near the surface of the section, and it is possible that the tops of them were eroded. Lastly, in the 3.5 km of reach I, reworked fluvial layers covered 1.5 m lacustrine deposits. We interpret this spatial distribution of Dagouwan Formation lacustrine deposits throughout the Salawusu River valley as representing at least five discrete paleo-lakes, ranging in length from 3.5 to 11 km, which were separated by aeolian dunes or

Table 1

AMS ^{14}C dating results of bulk organic material samples from GGZ, DSGW2020, and SCH sections.

Section	Depth (m)	Sample No.	Laboratory No.	Conventional ^{14}C ages (yr B.P.)	Reservoir-corrected ages (yr B.P., ±2σ)	Corrected calibrated ages (Cal.yr B.P., ±2σ)
GGZ	0	GGZ-AMS1	Beta-485,458	2260 ± 30	1730 ± 30	1600 ± 50
	0.50	GGZ-AMS2	Beta-504,593	3880 ± 30	3350 ± 30	3560 ± 80
	2.26	GGZ-AMS3	Beta-485,461	9740 ± 30	9210 ± 40	10,350 ± 100
DSGW	0	DS18-AMS1	Beta-579,399	2230 ± 30	1700 ± 30	1580 ± 50
2020	0.76	DS18-AMS3	Beta-579,400	3040 ± 30	2510 ± 90	2550 ± 60
	2.16	DS18-AMS10	Beta-579,401	10,170 ± 100	9640 ± 30	11,120 ± 60
	0	SCH-1	Beta-481,758	2970 ± 30	2440 ± 30	2450 ± 90
SCH	1.38	SCH-1LSB	Beta-504,594	5110 ± 30	4580 ± 30	5300 ± 30
	3.22	SCH-2	Beta-481,759	8070 ± 30	7540 ± 30	8370 ± 40

sand sheets along the top surface of the Salawusu river valley.

3.2. The lithology of typical Dagouwan Formation lacustrine deposits in the Salawusu River valley

The GGZ section (37° 42′27.3″N, 108° 28′9.69″E) is located on the left bank of Salawusu River (Fig. 3a, d). Its topmost part is a 0.8 m thick relatively homogeneous tillage layer, which is not discussed in this study due to possible human disturbance. The DSGW2020 section (37° 43′20.9″N, 108° 31′2.6″E) is located on the left bank of Salawusu River, about 5.5 km north of the GGZ section (Fig. 3b, e). SCH (37° 47′37.95″N, 108° 35′17.24″E) lies on the right bank of the Salawusu River, 11 km east of the DSGW2020 section (Fig. 3c, f). In the GGZ, DSGW2020, and SCH sections investigated in this work, the thickness of lacustrine deposits is 2.50 m, 2.16 m, and 3.22 m, respectively. They have comparable sedimentary properties in appearance in the field, with no visible indicators of hiatuses, and can be broadly separated into two lithological units from top to bottom: (1) The upper unit is primarily composed of grayish black to grayish white sandy silt with abundant calcareous concretions, with depths of 0–0.68 m, 0–1.12 m, and 0–1.38 m, separately; (2) The lower unit is composed of grayish-white to grayish-green silty sand with sporadic calcareous concretion, with depths ranging from 0.68 to 2.50 m, 1.12–2.16 m, and 1.38–3.22 m, respectively.

Full presentation of the particle size analysis results conducted on the three sections studied in detail for this study, as well as modern analogue facies, can be found in the Supplementary Materials, section S3.

3.3. Chronology

The new AMS^{14}C ages from the organic matter for the three sections are shown in Table 1. There is some broad consistency, but also some localized variation. The three ages from each section were in chronological order within a stratigraphic sequence (Fig. 6). The basal age at the GGZ section was 10,350 ± 100 cal yr BP, with the unit top dating to 1600 ± 50 cal yr BP. DSGW2020 began accumulating slightly earlier, at 11120 ± 60 cal yr BP, and an uppermost date constrains near-synchronous cessation of accumulation of lake sediment (the age here is 1580 ± 50 cal yr BP). The SCH section began accumulating later, at around 8370 ± 40 cal yr BP, with the cessation of accumulation of lake deposits occurring earlier, at around 2450 ± 90 cal yr BP. At each section, ages from the middle of the unit suggest broadly constant

accumulation, as much as can be inferred from three data points for each. Age-depth models were established by linear interpolation. Based on these models, the deposition rates for the GGZ, DSGW2020, and SCH, were 0.025 to 0.027 cm/yr, 0.016 to 0.076 cm/yr, and 0.048 to 0.060 cm/yr, respectively.

These age determinations are consistent with previous estimates of the onset of lacustrine deposits in the Salawusu river valley ranged between 13,500 and 8290 yr BP., according to the 41 ages previously published (Lu et al., 2010; Li et al., 2012; Liu and Lai, 2012; Zhao et al., 2016; Shu et al., 2016; Liu et al., 2018a). The termination of lacustrine activity from the new chronologies suggests a late Holocene date, whereas previous studies have varied very widely in this respect, from 8900 to 630 yr BP. Within the dating error, the GGZ and DSGW2020 sections, at least 5 km from one other, have similar commencing and terminating ages, indicating that both were accumulating between ~10,400- ~ 11,000 and ~ 1600 cal. yr BP. Though the GGZ section's dates revealed that its sedimentary record was slightly shorter, the ages suggest that it may have preserved most of the same sedimentary environmental information as the GGZ and DSGW2020 sections.

3.4. Chronologically-constrained physical and geochemical sedimentology

To facilitate comparison between the sections temporally, the age-depth models (Fig. 4a) were used to provide time-constrained sedimentology and geochemical records for the three sections. These are shown in Fig. 4.

All of the profiles reveal a marked difference in grain size properties between the early−/mid-Holocene sediments and those of the mid−/ late Holocene, with each demonstrating a large decline in the sand fraction (Fig. 4b). However, the nature and timing of this transition varies, with DSGW2020 characterized by a steady decline beginning almost at the base of the section; in contrast, at GGZ, the slow decline in sand content begins in the mid-Holocene at around 5.5 ka, whereas at SCH the decline is also around 5.5 ka, but is much more rapid. At just one site (DSGW2020), there is a final shift back towards sand-dominated sediment at the top of the section (after ~2 ka). The very low fraction of sands <80 μm (Fig. 4c) and mean grain size (Fig. 4d) confirms that not only is the abundance of the late-Holocene sand fraction much reduced, the grain size of this sand fraction is also reduced, to exclusively fine sands.

The geochemical characteristics, likewise, reveal some similarities

Fig. 3. Field photographs of the sections at a) GGZ, b) DSGW2020, and c) SCH sections with AMS ^{14}C ages of the sequences annotated. Locational context is provided for the section photographs for d) GGZ, e) DSGW2020 and f) SCH.
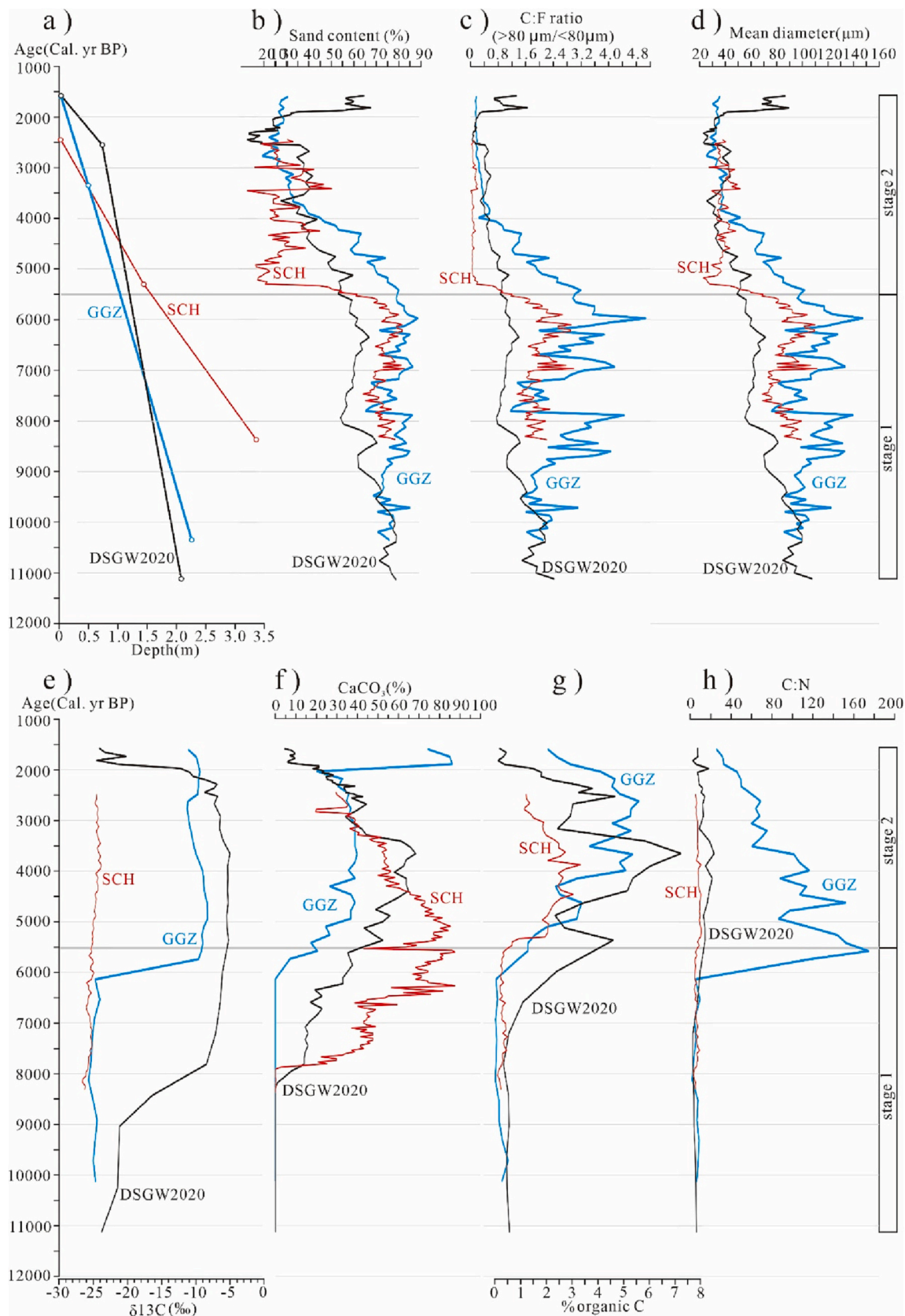
Fig. 4. Physical and geochemical characteristics of the detailed sections studied, plotted as a function of age. a) The age/depth models used to constrain the sections, b) sand content (> 50 μm), c) the coarse/fine ratio, defined around 80 μm (see Supplementary Materials S3), d) mean grain size, e) the δ¹³C isotope ratio, relative to the PDB standard, f) total percentage carbonate, g) percentage organic carbon and h) the carbon/nitrogen ratio.

between the profiles, but also substantial differences, in both lake behavior and timing. The $\delta^{13}C$ ratio for two of the sites (DSGW2020 and GGZ) is characterized by rapid early−/mid-Holocene excursions to much elevated values, though at different times (Fig. 4e); by contrast, no such excursion is seen at SCH. The $CaCO_3$ content shows a little more consistency between profiles (Fig. 4f), but still differences in the timings; each profile beings with negligible $CaCO_3$ at the start of the Holocene, but at varying times between ∼8 ka and 6 ka, shifts towards carbonate dominance in the sedimentation during the mid-Holocene. At DSGW2020 and SCH, this trend is reversed in the late Holocene, whereas at GGZ, carbonate dominance continues until the cessation of accumulation. The organic carbon records (Fig. 4g) show the most consistency, with all sections recording mid−/late- Holocene peaks in organic carbon at around 3.5–2.5 ka. The C:N ratio of the sections (Fig. 4h), however, again varies considerably between sections, with only the GGZ section showing a sudden and sustained shift towards much elevated values beginning around 6.5 ka. The interpretation and implications of these records is described in section 4.3.

4. Discussion

4.1. The spatial continuity of the Dagouwan Formation lacustrine deposition throughout the Salawusu river valley

Regional synthesis of the Dagouwan Formation lacustrine deposits show that, despite similar sedimentary sequences, the records do not relate to a single lake; at least five palaeo-lakes were separated by other deposits, most likely aeolian dunes, during the middle-early Holocene in the Salawusu river valley (Fig. 2). This supports the suggestions of Zhao et al. (2016), who posited that some of the difficulty in reconciling different sections within the DSGW might be due to the presence of several small lakes at different periods, rather than the Dagouwan Formation representing a single lake. Spatial analysis of the region at a wider scale confirms that this is the case, and several sections are identified in the valley in which lacustrine deposits are entirely absent (Fig. 2). Even where the lake deposits are found, the thickness of the Dagouwan Formation lacustrine deposits varies at different locations within these palaeo-lakes throughout the region. The Milanggouwan section, for example, is located on the fringe of the River Reach *E*-Paleolake 3 (Fig. 2), where the Dagouwan Formation lacustrine deposit is thinner and the sedimentary environment may be easily altered by local factors. Furthermore, in the DSGW meander of the Salawusu river, some lenticular bodies of oxbow lake associated with palaeo-river channels have been reported (Li et al., 2012; Zhao et al., 2016; Liu et al., 2018a) and also identified by this field investigation, which could result in the discontinuities of lacustrine deposits. These two observations perhaps help to explain why previously reported reconstructed paleoclimatic results differ (Lu et al., 2010; Li et al., 2012; Liu and Lai, 2012; Zhao et al., 2016; Liu et al., 2018a; Wang et al., 2021). The differing evolutionary history of the lakes represented by the GGZ, DSGW and SCH sections is explored in more detail in Section 4.3; we turn first, however, to the broader interpretation of these sequences with regard to the sedimentary characteristics of the lacustrine units.

4.2. Sediment sources and palaeoclimatic environmental implications

4.2.1. Sediment sources

Since the Salawusu River valley lies in a depression between the Mu Us Desert to the north and west, and the northern portion of Chinese Loess Plateau (Fig. 1) to the south and east, the deposits in the study area valley could originate from either, or both, of these areas. The modern-day landscape is a patchwork of active and semi-active aeolian dunes, land cleared for agriculture, and a meandering channel punctuated by reservoirs. The grain-size distributions of modern aeolian dune sands demonstrate that they are dominated by sand-size particles and have bimodal characteristics, with marked peaks of >80 μm and a lesser peak

of <80 μm (Supplementary Material; Fig. S4). The grain-size features of modern lacustrine sediments collected from low-lying seasonal lakes in the Salawusu River valley mainly consist of silt- and sand-size particles, displaying trimodal distributions, with major peaks of <80 μm and 80–1000 μm, and comparatively weak peaks of >1000 μm. The obvious peaks of 80–1000 μm for modern lacustrine sediments match those of modern dune sands in Mu Us Desert, indicating that the coarser particles of lacustrine sediments are mainly derived from aeolian dune sands. Fig. 5 also shows that sandy loess from the northern CLP is primarily composed of silt with marked unimodal peaks of <200 μm. The significant peaks of <80 μm for modern lacustrine sediments are overlapped with the predominant grain-size distribution of sandy loess, implying that the finer particles of modern lacustrine sediments originate from sandy loess in northern CLP. To put it another way, both aeolian sands (from the north/west) and sandy loess (from the south/east) appear to be the sources of modern lacustrine sediments in the Salawusu River valley. The grain-size characteristics of the Dagouwan Formation lacustrine deposits from the GGZ, DSGW2020, and SCH sections during the Holocene, as shown in Fig. 5 and Table 2, broadly resemble those of modern lacustrine deposits, but have fluctuated substantially during the Holocene, representing changing sediment supply pathways. The next section explores the palaeoclimatic implication of these changing pathways.

4.2.2. Transport pathways and mechanisms

Two broad mechanisms of transport – hydrologically or windblown - might be responsible for the erosion and transport of the sands and silts to the lakes of the Salawusu River valley, and both are evidently active within the region. To the north and west, the landscape is dominated by evidence of wind-driven, aeolian activity in the form of dunes; to the south and east, the dissection of the loess of the CLP is apparently dominated by run-off driven erosion.

The wind regime of the study site is affected by the seasonal influences alternately dominated by both the northerly EAWM and southerly EASM (Fig. 1). Both the northerly and southerly wind can theoretically bring about sand-size particles only if the speed is greater than the calculated Drift Potential (DP, using 6 m/s as the threshold for sand movement). The DP is closely related to resultant drift potential (RDP) and resultant drift direction (RDD), which were used to depict the magnitude and direction of sand-transporting wind as a sand rose (Mason et al., 2008). Present-day local prevailing wind directions are dominated by the northerly direction (Fig. 1), occupying 66.2% of the total in a year over the period 1973–2003, according to measurements of wind speed and wind direction from Wushenqi weather stations, located in the inner of Mu Us Desert (Paul et al., 2015). According to the wind rose diagrams of calculated Drift Potential (DP) in the Mu Us Desert, the frequencies of NNW, N, NW, and WNW directions are 21.2%, 19.5%, 15.4%, and 8.1%, respectively, totaling with 64.2% of northerly direction, from 1 August 2008 to 31 July 2011 (Pang et al., 2019). In the Mu Us Desert, sand roses from Otog Qi, Dongsheng and Yulin are also dominated by northwesterly winds in both 1973–1983 and 1993–2003 (Mason et al., 2008).

Although the southerly component of the wind regime is secondary, accounting for 15.6% of the total calculated DP, and the frequencies of SSE and SE directions are 8.6%, and 7.0%, respectively (Pang et al., 2019), we cannot discount entirely the possibility that southerly winds might have played a role in the formation of aeolian sands to some extent. However, the prevailing southerly Asian summer monsoon brings warm air and rainfall, and as a result of these favourable conditions, vegetation is more extensive to the south and east, making it more difficult to move and transport sand-size particles by southerly wind activities. In light of this, together with the much lower sand-sized fraction contained within the loess to the south and east of the Salawusu Valley, the contribution of aeolian sands from the prevailing southerly Asian summer monsoon is likely to be minimal.

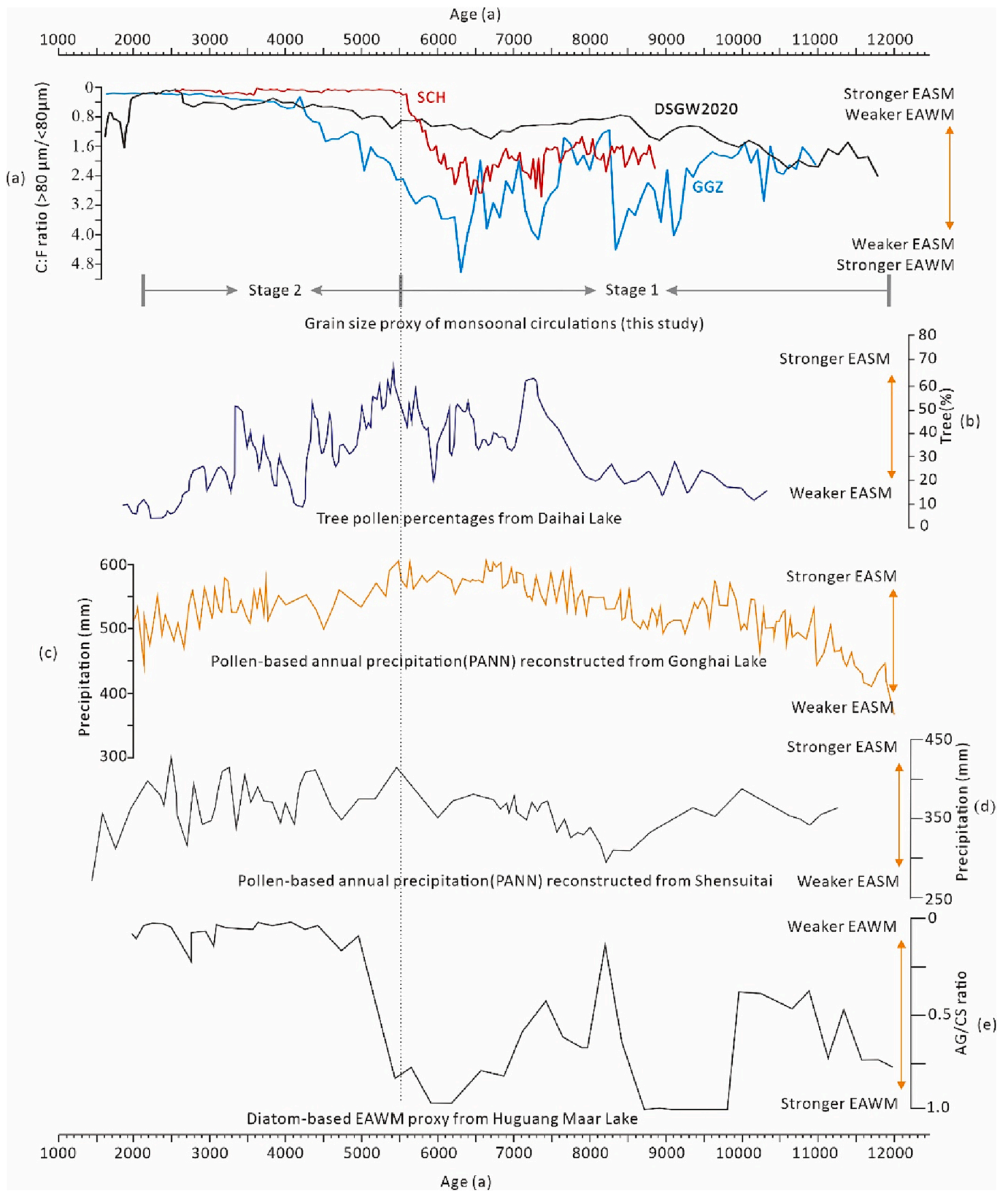Meanwhile, due to the lower amounts and the erratic nature of rain

Fig. 5. Summary of comparisons with the records reported from this study, and other regional lacustrine and peat records. (a) Comparison of grain-size CF ratio records from GGZ, DSGW2020, and SCH in the Salawusu river valley of Mu Us Desert with other records during the middle-early Holocene. (b) Tree pollen percentage from Daihai lake, Inner Mongolia, China (Xiao et al., 2004); (c) Pollen-based annual precipitation (PANN) reconstructed from Gonghai lake, Shanxi, China (Chen et al., 2015); (d) Pollen-based annual precipitation (PANN) reconstructed from Shensuitai, Mu Us Desert, China (Chen et al., 2023); (e) AG/CS (*A. granulata*/ *C. stelligera*) ratio from the Huguang Maar Lake, near the coast of the South China Sea (Wang et al., 2012).

Table 2

Grain-size components (%) and associated parameters for Dagouwan Formation lacustrine deposits and some samples from modern aeolian dune sands, modern shallow lakes in Mu Us Desert and loess of Chinese Loess Plateau. Note: VCS-CS (Very coarse sand and coarse sand, 2000-500 μm), MS (Medium sand, 500-250 μm), FS (Fine sand, 250-100 μm), VFS (Very fine sand, 100-50 μm); Silt (50-5 μm); Clay(<5 μm).

		Grain size fraction (%)						Mean grain size	Graphical moment statistics		
		VCS-CS	MS	FS	VFS	Silt	Clay	Mz (μm)	SD	SK	KG
GGZ	range	0–6.3	0.1–11.4	8.4–66.3	6.7–32.3	10.8–75.4	0.7–6.3	25–147	1.0–2.0	−0.3-0.6	0.6–2.2
(125)	mean	1.4	5.2	42.2	14.3	34.1	2.8	82	1.5	0.3	1.3
DSGW2020	range	0–1.7	0–6.39	2.1–55.0	7.8–23.7	20–83.6	1.1–13.0	23.1–107.6	1.1–2.1	−0.2-0.6	0.7–1.40
(108)	mean	0.3	1.9	31.5	16.3	46.0	4.1	56.4	1.5	0.2	0.9
SCH	range	0–4.6	0–5.8	0–59.4	7.4–42.4	16.5–85.2	0.8–5.2	23.2–111.6	0.8–1.8	−0.3-0.6	0.7–1.7
(161)	mean	0.30	2.1	30.7	20.3	44.5	2.1	64.8	1.3	0.4	1.1
Modern dunes	range	0–17	12.8–63.6	23.5–86.5	0–15.3	0–10.7	0–1.1	156–373	0.4–1.2	0–0.4	0.8–1.4
(20)	mean	4.3	38.4	50.8	3.5	2.8	0.3	257	0.7	0.1	1.1
Modern shallow lakes	range	0–12	3–12	11–29	7–25	43–55	1–3	53–80	1.5–2.2	−0.3-0	0.8–1.3
(8)	mean	7	7	17	18	49	2	64	1.9	−0.2	1.1
Modern loess	range	0	0–1.9	0–15.7	0–33.5	46.3–75.3	6.4–24.7	10.8–45.5	1.3–2.1	0.1–0.4	1.1–1.4
(11)	mean	0	0.4	6.8	21.0	60.5	11.3	30.7	1.6	0.3	1.3

to the north and west, and the high infiltration rate of sand, the necessary runoff generation for water-transported sediments over arid dunes is deemed implausible (Kidron and Yair, 2001; Wu et al., 2012). As a result, runoff-induced transportation by the prevailing southerly Asian summer monsoon is unlikely to transfer coarser particles from an aeolian dune. During the rainy season (from May to October), however, rainfall results in the formation of linear and planar runoff on the surface of loess to the south and east. Loess is well-known for being prone to erosion. Thick layers of aeolian sand-loess sediments dominate the northern Chinese Loess Plateau, which is dominated by silt-sized particles; for example, loess sediments collected from Jingbian are mostly made up of silt, with a lesser sand component (Table S2 and Fig. S4).

It is necessary, though, to also consider complicating factors in both aeolian and hydrologically-driven sediment transport components from both regions. Changes in monsoonal intensity of both the EAWM and EASM will bring about changes not only in the dominant wind regime, but also in precipitation, vegetation, and potentially weathering intensity. Although an enhanced hydrological regime driven by a strengthened EASM might promote silt run-off from the south and east, it might also be expected to promote vegetation in this semi-arid landscape. Recent studies suggest a marked increase in herb taxa in the dunefields to the north (Chen et al., 2023), and complex and temporally variable vegetation responses on the loess plateau to the south are well-recorded (e.g. the review of Zhao et al., 2009). Impacts on aeolian processes, too, are likely to be impacted by such changes. Similarly, although it is assumed here that silt is primarily loess-derived, a component as a result of weathering of sand particles cannot be entirely excluded. The role of desert landscapes in generating silt by weathering (so-called 'desert loess') has long been debated (e.g. Lancaster, 2020; Smith et al., 2002), and the Mu US sands have indeed been proposed as a source for the loess plateau via weathering (Wen et al., 2019). However, the rates of change evident in the sedimentology of the sections (Fig. 4), together with concomitant changes in chemical and isotopic properties suggest that differing sources is more likely than enhanced weathering regimes.

Notwithstanding these caveats, it is interpreted that the coarser particles (sand-size particles, especially the particles of >80 μm) from the Dagouwan Formation lacustrine deposits in the Salawusu river valley mainly originate from aeolian dunes to the north, transported by northerly wind activities triggered by EAWM. The finer particles (silt-size particles, especially the particles of <80 μm) are primarily transported from the sandy loess of the northern Chinese Loess Plateau by runoff triggered by the EASM. Thus the grain-size characteristics of the lacustrine deposits reflect fluctuations in the palaeo-EAM during the Holocene: the coarser particles were products of enhanced EAWM, and the finer fractions were products of strengthened EASM. Thus the coarse: fine (C:F) ratio (>80 μm particles/<80 μm particles) can be used as an

index to represent the relative strength of EAWM vs EASM.

4.3. Synthesis of the lacustrine records

The picture that emerges, from twenty sections examined along the Salawusu River, many of which exhibit the same geological unit – the Dagouwan Formation lacustrine deposits - and three closely examined sections within ~15 km of each other, is complex. There is much consistency – for instance, similar Holocene lacustrine units outcrop at fifteen of the twenty sections over a distance of ~45 km (Fig. 2). All of the three sections studied in detail, using physical and geochemical sediment analysis in this study, show broadly consistent accumulation histories, beginning in the early Holocene and continuing until ~2.5–1.5 ka. Each begins with sand-dominated sedimentation, and switches to silt-dominated accumulation in the late Holocene. During the mid−/late Holocene, each experienced periods dominated by carbonate sedimentation, and each had organic carbon at its maximum at around 3.5–2.5 ka (Fig. 4).

Yet each of the sections also shows marked variability from the others in one or more property, despite it being likely that two of the sections (DSGW and GGZ) represent the same lake for much of their depositional history, and a maximum of ~15 km between. At DSGW and GGZ, the shift to silt-dominated sedimentation is gradual, but at some point during this transition is also reflected in a carbon isotope signature, which changes rapidly from levels reflecting local vegetation to much elevated values characteristic of inorganic carbon from the loess to the south (Fig. 4). At SCH, however, the shift from sand to silt domination is much more sudden (at around 5.5 ka), and yet there is no concomitant change in isotope values, which remain low throughout. At GGZ, C:N ratios of the sediment indicate a sudden shift towards terrestrial carbon input at around 6 ka; at the other sites, this signal is later and much more muted. Lastly, and only at the DSGW section, the final phase of lake accumulation reverts to sedimentation very similar to that of the early Holocene; sand-dominated and with a vegetation-dominated carbon isotope signature.

Some of these variations between sections may be explained by consideration of the spatial arrangement of the section, and their likely changing interconnectedness. For instance, if the accumulation of carbonate to these systems is indeed associated with increased loess contribution due to enhanced mid-Holocene EASM as we postulate here, it may make sense that this signal accumulates first downstream at SCH, and propagates upstream, affecting DSGW later (and to a lesser degree), and lastly GGZ. It is noticeable that the late-Holocene decline in carbonate sedimentation follows the same spatial pattern, with SCH responding first, followed by DSGW and lastly GGZ; although at GGZ, there is then a final phase dominated by carbonates again. Other changes are less easily explained in this way; for instance, the carbon

isotope trend towards an inorganic C signal does not follow the same spatial trend, despite the cause of both likely resulting from increased loessic silt input. The isotope record, more than any other parameter seems indicative of threshold effects at work, with both DSGW and GGZ responding suddenly, albeit it at two different times, separated by more than two thousand years. The reason for the lack of a similar δ^{13}C isotope trend at SCH remains unclear.

In summary, many of the trends in physical and geochemical proxies, which might have possible palaeoclimatic interpretation, only make sense when considered alongside the geomorphological setting of the lake basin(s). If examined in isolation, it might be tempting to ascribe regional palaeoclimatic inferences to many of the proxies for each of the three profiles studied here, and yet we show here that the records preserve some dramatically different characteristics than cannot be climatic in origin, due the proximity of the different sections.

4.4. Holocene palaeoclimatic and environmental change inferences

The records are consistent with an early Holocene dominated by relatively enhanced northerly/westerly circulation (i.e. EAWM relatively more effective at this location than the EASM circulation). There is some evidence (e.g. carbonate sedimentation at DSGW and SCH, increased silt input at DSGW) of enhanced EASM efficacy from around 8 ka. However, more consistent evidence at all three sections of heightened EASM activity dates postdates 5.5 ka (e.g. silt-dominated accumulation, increased organic carbon and carbonate sedimentation associated with loessic input under more southerly circulation). It is notable that most lines of evidence for this enhanced circulation do not decline until around 2 ka.

Despite the local differences in profiles, general characteristics allow the delineation of two distinct and consistent stages, before and after 5.5 ka (Fig. 4):

Stage 1 (11.1 to 5.5 ka): For the majority of samples, the sand content ranges from 55% to 90%, the content of >80 μm particles from 40% to 90%, the C:F ratio from 2.20 to 4.80, and the mean diameter (μm) from 55 to 150 μm; the silt content ranges from 10% to 45% and the content of <80 μm particles from 10% to 55%. The first four grain-size proxies have much higher values, indicating a stronger EAWM; whereas the latter two grain-size proxies have significantly lower values, suggesting a weaker EASM.

A lake formed at the DSGW section at ~11.1 ka, and began accumulating lake sediments at 1271 m elevation. This occurred at a time of increased sand mobility in the Mu Us to the north (Lu et al., 2005), coincident with reduced EASM penetration, according to both speleothem records from southern China and terrestrial records from northerly sites (Liu et al., 2015). Zhao et al. (2016) demonstrate clearly that the regional gradient of the Salawusu valley region precludes the development of a single mega-lake, and there is no compelling evidence for increased moisture availability at this time on which to infer a precipitation-based cause for the lake's formation. We thus concur that the accumulation at DSGW likely resulted from geomorphological changes; most likely drainage rearrangement as a result of aeolian sand movement across the valley. Sedimentation at DSGW was sand-dominated (~80%), and there was no carbonate deposition (Fig. 4b and f). What little organic carbon there was (<1%) shows a C:N ratio consistent with an aquatically-dominated vegetation signal (~8–10:1) and a carbon isotope ratio of ~ − 25‰, consistent with a C3-vegetation dominated signal (e.g. Parker et al., 2004) (Fig. 4e, g and h).

At around 10.4 ka, lake sedimentation began at GGZ, around 4.7 km upstream of DSGW, and at 1282 m elevation, around 10 m higher. The Dagouwan Formation is not exposed continuously along the valley side and the valley floor is extensively modified for modern-day agriculture; although there are no major topographic obstructions between the two sites, it cannot be conclusively determined if the lake accumulation at GGZ represents same lake as that which outcrops at DSGW. If it was part of the same lake, and represents the transgression upstream of the same

deepening and expanding lake system, and its extension into a side-valley of the main Salawusu, by 10.4 ka, the lake at DSGW was presumably at least 10 m deep. If, however, the two represented distinct lake basins with a fluvially-connected system, no estimates of lake depth can be made from these data, and it is inferred that the lake at GGZ began to fill as a result of topographic obstruction of the valley, or fluvial reconfiguration. Again, this model avoids the need to infer increased precipitation at a time when northern Chinese records suggest that the EASM is still reduced (Liu et al., 2015). Sedimentation at GGZ initially mirrored that at DSGW – sand-dominated (also ~80%), with no inorganic carbonate, very low organic carbon and an aquatically-controlled C:N ratio (Fig. 4b-h). The δ^{13}C ratio at the base of the GGZ section is also ~ − 25‰, though it is noticeable that by 10 ka, the ratio at DSGW had begun to increase, to around ~ − 22‰ (still within the range of C3 vegetation).

Between 10.4 ka and 8.4 ka, sedimentation continued in a similar vein, although DSGW began a decline in the sand fraction, to be replaced by an increasing silt fraction. At around 8.4 ka, lake deposits began accumulating at SCH, 10 km downstream from DSGW. At present, the reach in between these two sites is dominated by the dunes of the Mu Us Desert, encompassing both bands of the river, and at two sections (Fig. 2) of this reach, surveyed profiles graded from aeolian sands to black sandy soils with no trace of the Dagouwan Formation lacustrine unit. For this reason, we attribute the initiation of accumulation at SCH to a further blockage of the drainage, immediately downstream of the section. Despite similarities in sediments, there is no reason to require the lake which formed the DSGW and GGZ sections, and that at SCH, to be the same, though it is possible that some hydrological connectivity may have remained. The initial lake deposits at SCH are effectively indistinguishable from those that began to accumulate at DSGW and GGZ – sand-dominated (~70–80%), devoid of carbonates, low in organic C, with a δ^{13}C of around −25‰ (Fig. 4b-h). Coincident with the onset of accumulation at SCH, however, were some major, and diverse, changes to the accumulation at both DSGW and GGZ. The silt contribution at DSGW, which had been rising for at least two thousand years, rapidly increased, to be dominant (~60%), and the carbon isotope signature began a marked positive excursion, initially to around −17‰. Whilst it may be tempting to ascribe this to a change in vegetation type, towards more arid-adapted C4 types, the initiation of carbonate sedimentation at DSGW, coeval with the much-increased silt content, suggests instead a change of sediment source. Although a little earlier than many records suggest, this is broadly coincident with evidence for increased EASM activity (e.g. 8.6–7.8 ka synthesized by Liu et al., 2015), and likely reflects an increased sediment contribution, reworked from the carbonate-rich CLP to the south and east. The contribution from the low inorganic δ^{13}C values of the loess, typically −1 - -7‰ (Liu et al., 2011), would explain the rapidly rising isotope ratio at DSGW.

Different changes became apparent in the three established sections, assumed to represent at least two distinct lakes, at around 8 ka. The rise in isotope ratio at DSGW continued (to > − 10‰), although both GGZ and SCH maintained levels typical of a local vegetation signal during this period. The most dramatic changes, however, came at GGZ, in the form of an order-of-magnitude increase in the C:N ratio (suggesting the dominance of terrestrially-derived C), and at SCH where, within 500 years of lake sediment accumulation beginning, carbonate levels rapidly rose to around 40%. Thus, by 7.5 ka, each of the sections now showed very different limnological properties. DSGW was silt-dominated, with an isotope signature consistent with much-increased contribution of loess from the south and east, as well as showing the onset of carbonate sedimentation (around 20%); at GGZ and SCH, sand remained the dominant component, but at GGZ the system was now dominated by a terrestrial C component, and SCH was well on the way to becoming a carbonate lake.

The next major shifts in sedimentation at the three sections occurred at around 6 ka, in a period widely recognised (e.g. An et al., 2000) to be characterized by an enhanced EASM, and again, the sedimentary regime

at the different sections was varied. The carbonate content at DSGW increased further (to around 40%), likely reflecting the accumulation of carbonate-rich loessic silts, although this was coincident with an increase in organic carbonate, and a shift towards higher C:N ratios, which is interpreted to reflect increased terrestrial vegetation contribution. Shortly after a peak in the coarse (sand) fraction at both GGZ and SCH, and during a period of increasing silt deposition, the isotope ratio at GGZ shifted dramatically, echoing the change that had occurred at the DSGW section two thousand years previously. At the same time, the first evidence of carbonate accumulation began at GGZ, rising rapidly after 6 ka to around 40% a millennium later. The section at SCH at this point testifies to a true carbonate lake, with values in excess of 80% shortly after 6.5 ka (Fig. 4f). At all three sites, 6–5.5 ka marks the start of a mid-Holocene rise in organic carbon (Fig. 4g).

Stage 2 (5.5 to 1.6 ka): Although the different systems are characterized by changing environmental conditions at different times, rates and magnitudes, 5.5 ka provides perhaps the best point to distinguish between early and late-phase accumulation at the sites. High silt percentages and the amount of <80 μm particles dominate this stage, with most samples ranging from 40% to 90%, indicating a stronger EASM. The sand content, >80 μm particles, C:F ratio, and mean diameter (μm) were all significantly lower than in stage 1, with most samples ranging from 10% to 45%, 0 to 40%, 0.10 to 1.60, and 20 to 70 μm, indicating a weaker EAWM. Under these circumstances, the EAWM would be considerably weaker than the normal in the winter-spring seasons, while the EASM would be much stronger in the summer-autumn of the same year. Likewise, given these conditions occurred year by year during Stage 2 (5.5 to 1.6 ka), the climate would be more humid, resulting in a higher lake level; and aeolian activity would be limited. The lowest sand concentration and the most <80 μm particles are found between 5 and 2 ka, indicating the least frequent aeolian activity and the strongest EASM through the Holocene in the Mu Us desert.

The most dramatic change at this time was the sudden shift at SCH from values of around 80% sand, which had characterized it since its formation, to around 80% silt (Fig. 4b-d). Accumulation of sands at GGZ began a much slower decline at around the same time, but essentially, after 6 ka, all three sections had switched from sand-dominated lacustrine systems to silt deposition. Similarly, between 5 and 2 ka, all the sections experienced peaks in organic carbon, and each showed shifts towards higher (>10:1) C:N ratios. Although only SCH perhaps attained true carbonate lake status around this mid−/late-Holocene period, deposition was substantial (>40%) at both DSGW and GGZ. However, perhaps the most surprising trend from this period, is not a dramatic shift, but the precise opposite; the carbon isotope ratio at SCH, rather than mirroring the sudden shifts to elevated values seen at both DSGW and GGZ during the early−/mid-Holocene remained at values characteristic of a vegetation-dominated signal, at around 25 ‰.

Although many aspects of the sedimentation remained consistent during the interval 5 to 2 ka, with silt-dominated grain sizes, increased carbonate concentrations, increased organic carbon and increased terrestrial carbon at all three sites, and an isotope signature characteristic of loess-derived input at DSGW and GGZ, after 2 ka several final changes occurred before the final cessation of lacustrine sedimentation. The first, constrained by an uppermost date of 2.5 ka, was the termination of accumulation at SCH. The lake appears to have drained, likely the result of the breaching of the obstruction that caused the lake to form, something perhaps hinted at in the prior decline in carbonate deposition; by its end, the lake at SCH was no longer a carbonate lake, with values of ~20–40%. At DSGW and SCH, however, the lake persisted for at least another thousand years, but with a couple of major shifts again in sedimentation style. At DSGW at around 2 ka, sedimentation reverted to sand-dominance (Fig. 4b-d), coincident with a sudden drop in the δ13C isotope values, and broadly coincident with a marked increase in accumulation rate (Fig. 4a). In its final stages, the lake at DSGW operated much as it had at its inception in the early Holocene; this would suggest a strengthening of the EAWM at around this period,

although human impact on the landscape cannot be discounted at this stage (e.g. Sun, 2000). At around the same time, at GGZ, however, it was not the grain size that changed, but a sudden step-change in the carbonate production, to around 80–90% (Fig. 4f). For the last ~800 years or so of its existence, the lake at GGZ was a carbonate lake. The upper boundary of the Dagouwan Formation at GGZ is capped by agriculturally-derived meadow soils, and it is possible that this boundary is disconformable, and that the uppermost section of the unit is missing. However, given the elevation differences between GGZ and DSGW, this is not likely to represent a substantial period of time. When the lake finally drained, it did so quickly, given the coeval abandonment dates at two sections, ~5 km apart and ~ 10 m different in elevation.

4.5. Comparison with other palaeoclimatic records of the Mu US

The Dagouwan Formation lacustrine deposits preserved the history of a drier stage 1 (11.2 to 5.5 ka), dominated by a stronger EAWM. Although there was sufficient precipitation for lakes to fill, the absence of fine-grained sediment from the south and east implies a reduced efficacy of the EASM. Here we consider the records (Fig. 5a and 6a) in the context of selected other records of both EASM and EAWM monsoonal intensity from the wider region, noting that the inter-relationship between the two monsoonal circulations is not necessarily a bipolar one, and maybe indeed have varied over time (Steinke et al., 2011; Xia et al., 2014).

4.5.1. Lacustrine and peat records

Arid herbs and shrubs dominated the lake basin of Daihai, 450 km to the northeast of the Salawusu river valley, from ~10.25 to 7.9 ka, indicating mild and dry climatic conditions (Xiao et al., 2004) (Fig. 5b). This record has been interpreted to primarily reflect EAWM conditions in terms of temperature and EASM in terms of moisture availability, and thus suggesting reduced impact of both monsoons during the early Holocene. Another EASM proxy record, the pollen-based annual precipitation (PANN) reconstructed from Gonghai lake, 300 km to the ENE of the present study area, portrayed a progressive increase from 400 mm at 12 ka to 500 mm at 7 ka (Chen et al., 2015) (Fig. 5c). Recent PANN reconstruction from a section closer to the Salawusu River Valley (80 km to the NE) also suggests a reduced moisture availability, and thus EASM, during the interval 11.2 to ~8.3 ka (Fig. 5d; Chen et al., 2023). Despite the very substantial spatial distance (1800 km to the south, and thus likely experiencing differences in timing and magnitude of changes), the Huguang Maar Lake is significant as the AG/CS (*Aulacoseira granulata/Cyclotella stelligera*) diatom ratio from is explicitly interpreted as a proxy for the EAWM (Wang et al., 2012). Here, the high AG/CS ratio is interpreted as a generally robust EAWM between 13 and 5 ka (Fig. 5e). Elsewhere is the Mu Us Desert, despite the development of several layers of sandy palaeosol during the early Holocene (11.5 to 8 ka), the relatively weak weathering and pedogenesis suggest that the East Asia Winter Monsoon was still active at the time (Mason et al., 2009; Yang et al., 2019).

Stage 2 (5.5 to 1.6 ka) was the more humid phase, with the weakest activity led by a stronger EASM alternating with comparatively weaker EAWM (Fig. 5a). This stage might roughly be taken as the "Holocene Optimum" period (~8.5–3 ka) with a stable warm and wet interval (between ~7.2–6 ka), as defined by Shi et al. (1993). Indeed, a shift towards fine-dominated sedimentation had already begun by 7 ka in the GGZ section. This comparatively late onset for the strengthened mid-Holocene EASM, however, is echoed by the timing of the pollen record from Daihai Lake was characterized by a warm and moist environment, from 7.9 to 4.5 ka, indicating that the wettest climate and heaviest summer monsoon occurred between 6.1 and 5.1 ka (Fig. 5b; Xiao et al., 2004). Other records from the region might also suggest a slightly earlier onset of more humid conditions; at Gonghai Lake, the PANN reconstructions (Fig. 5c) suggests a steady increase in precipitation throughout the early Holocene, with peak precipitation occurring
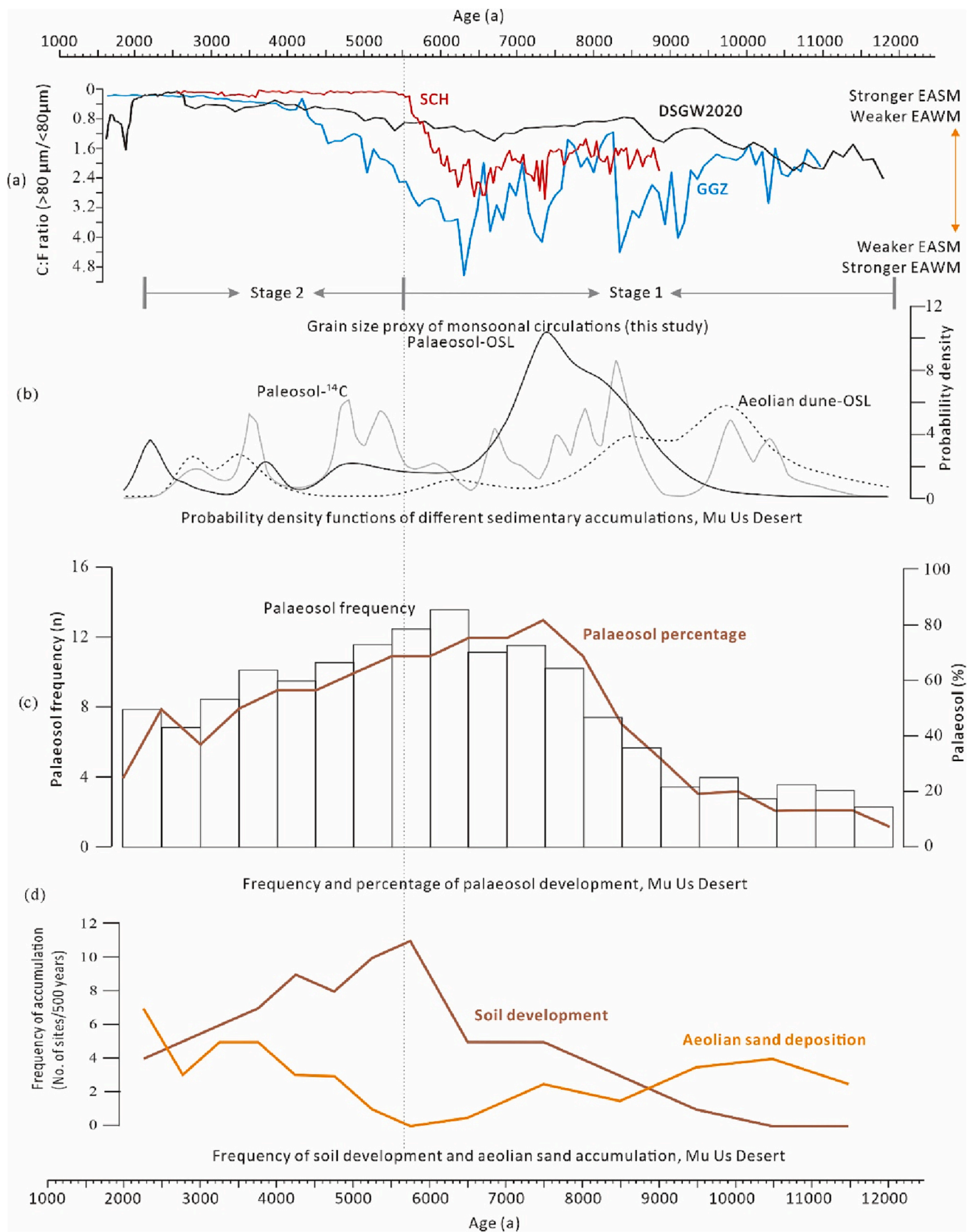
Fig. 6. Summary of comparisons with the records reported from this study, and other regional aeolian records. (a) Comparison of grain-size CF ratio records from GGZ, DSGW2020, and SCH in the Salawusu river valley of Mu Us Desert with other records during the middle-early Holocene. (b) Probability density plot for the OSL and ^{14}C ages of aeolian and paleosols from the Mu Us Desert (Jia et al., 2015); (c) Frequency and percentage of palaeosol development within the Mu Us Desert as synthesized by Liu et al. (2022); (d) Frequency of dune aeolian deposition and dune stabilization (i.e. soil development), plotted for the Mu Us region from data in the Supplementary Materials of Xu et al. (2020). Note that the bin width change from 500 years to 1 ka at 6.5 ka and data are normalized accordingly.

~7- ~ 4 ka. The Shensuitai PANN record (Chen et al., 2023) also shows an increase in precipitation from around 8 ka onward (Fig. 5e). Again, noting the caveats associated with the large spatial interpolation, the EAWM diatom proxy ratio of AG/CS (*A. granulata/C. stelligera*) from the Huguang Maar Lake, decreased after 5 ka, indicating a major decline in the EAWM (Fig. 5f: Wang et al., 2012).

4.5.2. The aeolian records

It seems relevant, given the hypothesized role of aeolian sedimentation of sands in affecting the hydrological connectivity of the basins to explicitly consider the records of aeolian accumulation from the Mu Us Desert. The region was one of the first in China to have luminescence dating applied to develop aeolian chronologies (e.g. Lu et al., 2005; Sun et al., 1998), although the widespread development of palaeosols within the dunes had already permitted more 14C-based chronologies than in many other desert regions. By 2019, 136 luminescence ages were reported for the Mu Us Desert (Guo et al., 2018; Lancaster et al., 2016), and more have been published since. Whilst noting some of the caveats associated with this form of analysis (e.g. Telfer and Hesse, 2013; Williams, 2012), this section compares dated evidence from aeolian deposits with the Salawusu lacustrine record presented in this study (Fig. 6a).

The synthesis of dated terrestrial sample probability densities from the Mu Us Desert of Jia et al. (2015) (Fig. 6b) shows aeolian deposition exhibited a peak in frequencies during the early Holocene (12 to 8 ka), coincident with the onset of lacustrine accumulation at the Salawusu Valley records presented here. The same review (Fig. 6b) suggests a decline in aeolian sedimentation, and an increase in both radiocarbon and luminescence ages on units interpreted as palaeosols comparatively early, by around 8.5 ka (peaking at around 7. 5 ka), although aeolian accumulation continued coincident with soil development – an idea that has since been reinforced, especially by Xu et al. (2020). Notwithstanding some likely overlap with Jia's earlier summary, due to some of the same data being incorporated in both analyses, Liu et al. (2022) also suggested a peak in soil formation around 7.5 ka for the Mu Us region. However, a recent set of analyses of both existing and new sites in the Mu Us dunefields (Xu et al., 2020) (Fig. 6d) not only suggests a later peak in soil formation at around 6 ka, and thus close to the periods of maximum change in the Salawusu records presented in this study, but crucially perhaps notes that there is very clear evidence for coeval aeolian accumulation and soil development. That is, at a localized scale, active dunes and stabilized dunes undergoing pedogenesis can coexist. This is significant for this study, as it suggests that throughout very much of the Holocene, excluding perhaps a brief interval in the mid-Holocene, aeolian sand movement and deposition has been possible, with the potential to act as a mechanism for hydrological disturbance; it is notable that the periods of maximum proposed aeolian sand movement coincide respectively with the onset and termination of the lacustrine records at many of the Salawusu sections.

This pattern is broadly matched by a wider trend in the eastern portion of the desert belt in northern China; between approximately 8.6 to 3.2 ka, there was an increase in the frequency of palaeosol development and a decrease in aeolian-sand activity (Yang et al., 2019). The aeolian sands were gradually consolidated and the paleosols were widely distributed between 8.5 and 4 ka (Mason et al., 2009; Jia et al., 2015). Numerous palaeosols developed on the Chinese Loess Plateau between 8.8 and 3.4 ka, showing a generally strong EASM (Wang et al., 2014). More recent and wider synthesis of dune palaeosol development in the Chinese dunefields by Liu et al. (2022) suggests a continent-scale asymmetry in the onset of soil formation, similar to that originally proposed by An et al. (2000).

Aeolian deposits also have potential to preserve other proxies of palaeoclimate within them, and as a result of the relatively high carbon content of the dune sands of the Mu Us, some have focused on the stable isotope record contained within. In the light of the very dramatic shifts in isotopic ratios seen at some – but not all – of the sections studied here,

some consideration of the aeolian isotopic record is justified. Although sometimes characterized by low temporal resolution, these have nonetheless suggested a mid-Holocene increase in moisture availability on the ground of changing $\delta^{13}C$ ratios (Lu et al., 2012). To obtain sufficient samples to overcome temporal limitations in the aeolian record, large-scale regional syntheses have been compiled (Guo et al., 2019), but the net result shows little clear systematic trend during the Holocene, and the likely impact of local factors, once again emphasizing the potential complexity of the (vegetated) landscape response to change.

4.5.3. Synthesis

The different proxy records, from different sections, presented here also help resolve some issues regarding the timing of Holocene monsoonal changes. According to a much-discussed hypothesis proposed by An et al. (2000), the strengthening of the EASM was asynchronous throughout central and eastern China, reaching a maximum at different times in different places, based on the spatial and temporal distribution of Holocene monsoonal precipitation determined from geological data. The sedimentary data presented here suggest that the peak in the EASM circulation in the Salawusu River valley of the Mu Us Desert was between relatively late, between ~5.5 and 1.6 ka; significantly later than the 11–7 ka (uncal.) proposed on the basis of lake level synthesis (An et al., 2002). However, the assumption made for lakes in this region by An et al. (2002) was that most of the lakes in the region are in closed basins and acts as "natural precipitation gauges"; the present study suggests that lakes in the region may well have been hydrologically connected, and moreover that this hydrological connectivity changed over time, complicating synthesis. Recently, vegetation and soil moisture feedbacks have been suggested to account for the apparently lagged vegetation response to rainfall (Cheng et al., 2021). The data presented here (Fig. 4), which offer insight into the timing of the monsoonal circulations without necessarily requiring interpretation of vegetative response suggests that the comparatively late development of the enhanced Holocene EASM does not necessarily require this biogeographical feedback.

5. Conclusions

Field and laboratory investigations of Holocene lacustrine deposits (the Dagouwan formation) outcropping along ~45 km the Salawusu River valley in north central China have synthesized numerous sequences, in order to resolve conflicting interpretations revealed in the literature, typically from single-section studies. The importance of the site lies in part in its location at the interface of the EAWM and EASM, and the distinct sediment types to the north/west and south/east, which offer the prospect of the record of varying summer and winter monsoonal strength during the Holocene. In addition to the general stratigraphy of twenty sections in total, three sections were studied in detail for physical sedimentology and geochemical characteristics, with new geochronometric assays. Although some similarities exist between both the regional stratigraphies and the detailed sections, there is also marked spatial variation in the extent of the deposits, and the physical and chemical characteristics of the lake sediments.

The lack of spatial continuity of the Dagouwan Formation is consistent not with the deposits representing a single lacustrine unit, and although some earlier studies implied a single extensive Holocene palaeolake in the region (e.g. Liu and Lai, 2012), synthesis of the records here suggests at least five sections of palaeolake(s), separated by aeolian dunes. This supports the assertions of Zhao et al. (2016), because of regional topography, that the Dagouwan Formation cannot be taken to be indicative of a single lake. Past discrepancies between palaeoclimatic records in the region have been varying attributed to chronological uncertainties (e.g. Liu and Lai, 2012) and catchment-specific parameters (Liu and Lai, 2012; Zhao et al., 2016). On the basis of the regional synthesis of the sections, the data presented here strongly support the hypothesis that numerous lakes, of unclear hydrological connectivity,

existed during the Holocene. The widely differing dates for the onset of accumulation reported from previous studies (Fig. 2), as well as the sections studied here (with internally consistent methodology), strongly suggest that different lakes within the valley have appeared and ceased at different times throughout the Holocene. This recognition of multiple basins and evidence for differing periods of accumulation strongly casts doubt of the direct palaeoclimatic implications of the presence or absence of the lake (i.e. equating the onset of lacustrine accumulation directly with a wetter climate; e.g. Liu and Lai, 2012). Even considering differences between the chronologies and proxies (e.g. assumptions, methods), the synthesis here suggests that the climate has been sufficiently humid in the Salawusu valley to permit lake formation at any interval from perhaps 11 ka to as recently as ~1.5 ka. Whether or not a lake formed at any given point at any given time during the Holocene likely depends more on fluvio-lacustrine and aaeolian geomorphology than climate.

A further reason that has been suggested (e.g. Zhao et al., 2016) to account for past differences in interpretation in the palaeoclimatic records of the region has been the misinterpretation – or perhaps more cautiously, inconsistent interpretations of different proxies – of the sedimentary record. Here, by employing consistent methodology at three sections, close enough together that the palaeoclimatic forcing must be consistent, we can directly address this question. Despite the consistent methodology, very substantial differences in almost all of the physical and geochemical parameters investigated here exist between the different sections. Whilst some of the more minor differences exhibited (e.g. the timing of the onset of carbonate accumulation, or the timing of the late-Holocene peak in organic carbon) could conceivably be accounted for by errors in the age-depth model, this cannot account for all changes. Dramatic differences in the timing and magnitude of changes (or lack thereof) in the $\delta^{13}C$ isotope regime, the ratio of fine: coarse clastic input, the carbonate content and the C:N ratio can only be explained by highly localized differences in palaeolimnological behavior. Not only does the Dagouwan Formation represent sediment accumulated from numerous individual palaeolakes, but in many respects, these palaeolakes behaved very differently, despite their proximity to each other. With regard to the question of hydrological connectivity of individual basins, raised earlier, this observation suggests that in many cases, this is limited. The inference is clear, however; studies attempting regional inferences from single-section and single-proxy studies will be unable to dissociate regional palaeoclimatic and localized geomorphological and palaeolimnological effects. This lesson is relevant not just to this region, but to all similar sequences in which large-scale connectivity and thus similar sedimentological responses to climate might be assumed.

Despite these differences, some consistencies between the sequences are sufficient that the locational advantages of the Salawusu River valley deposits can be used to infer broad trends in the monsoonal regimes of the EAWM and EASM. The early−/mid-Holocene (~11.2–5.5 ka) are characterized by an enhanced EAWM circulation, bringing increased aeolian sand input from the Mu Us desert to the north and west. This declined, coincident with an enhanced EASM, sometime by ~5.5 ka, and these conditions dominated the mid−/late- Holocene until the first evidence of weakening EASM at around 3 ka, and the final cessation of the lacustrine records between 2.5 and 1.6 ka.

Declaration of Competing Interest

The authors declare the following financial interests/personal relationships which may be considered as potential competing interests: Xiaohao Wen reports financial support was provided by National Natural Science Foundation of China. Xiaohao Wen reports was provided by China Scholarship Council.

Appendix A. Supplementary data

Supplementary data to this article can be found online at https://doi.org/10.1016/j.palaeo.2023.111580.

References

An, Zhisheng, Porter, Stephen C., Kutzbach, John E., Xihao, Wu, Suming, Wang, Xiaodong, Liu, Xiaoqiang, Li, Weijian, Zhou, 2000. Asynchronous Holocene optimum of the East Asian monsoon. Quat. Sci. Rev. 19 (8), 743–762.

An, Z.S., Kutzbach, J.E., Prell, W.L., Porter, S.C., 2001. Evolution of Asian monsoons and phased uplift of the Himalayan Tibetan plateau since Late Miocene times. Nature 411 (6833), 62–66.

Bascomb, C.L., 1961. A calcimeter for routine use on soil samples. Chem. Ind. 45, 1826–1827.

Beta Analytic, 2022. Beta Analytic Standard Pretreatment Protocols. Available at: http://www.radiocarbon.com/pretreatment-carbon-dating.htm#Washes (Accessed 10 Jan 2022).

Burke, C., Stott, P., 2017. Impact of anthropogenic climate change on the East Asian Summer Monsoon. J. Clim. 30 (14), 5205–5220.

Chen, Fahu, Xu, Qinghai, Chen, Jianhui, John, H., Birks, B., Liu, Jianbao, Zhang, Shengrui, Liya, Jin, An, Chengbang, Telford, Richard J., Cao, Xianyong, Wang, Zongli, Zhang, Xiaojian, Kandasamy, Selvaraj, Lu, Houyuan, Li, Yuecong, Zheng, Zhuo, Wang, Haipeng, Zhou, Aifeng, Dong, Guanghui, Zhang, Jiawu, Huang, Xiaozhong, Jan, Bloemendal, Rao, Zhiguo, 2015. East Asian summer monsoon precipitation variability since the last deglaciation. Sci. Rep. 5, 11186. https://doi.org/10.1038/srep11186 (2015).

Chen, D., Lu, R., Liu, X., Ding, Z., 2023. Holocene vegetation and climate reconstructions from pollen records in the Mu Us Sandy Land, China'. CATENA 220, 106698.

Cheng, J., Wu, H., Liu, Z., Gu, P., Wang, J., Zhao, C., Li, Q., Chen, H., Lu, H., Hu, H., Gao, Y., Yu, M., Song, Y., 2021. Vegetation feedback causes delayed ecosystem response to East Asian Summer Monsoon Rainfall during the Holocene. Nat. Commun. 12 (1), 1843.

Clemens, S.C., Prell, W.L., Sun, Y.B., 2010. Orbital-scale timing and mechanisms driving Late Pleistocene Indo-Asian summer monsoons: Reinterpreting cave speleothem delta O-18. Paleoceanography 25.

Ding, Y.H., Chan, J.C.L., 2005. The East Asian summer monsoon: an overview. Meteorog. Atmos. Phys. 89 (1–4), 117–142.

Folk, R.L., Ward, W.C., 1957. Brazos River bar—a study in the significance of grain size parameters. J. Sediment. Petrol. 27, 3–26.

Guo, L., Xiong, S., Yang, P., Ye, W., Jin, G., Wu, W., Zhao, H., 2018. Holocene environmental changes in the Horqin desert revealed by OSL dating and δ13C analyses of paleosols. Quat. Int. 469, 11–19.

Guo, L.C., Xiong, S.F., Dong, X.X., Ding, Z.L., Yang, P., Zhao, H., Wu, J.B., Ye, W., Jin, G. Y., Wu, W.W., Zheng, L., 2019. Linkage between C-4 vegetation expansion and dune stabilization in the deserts of NE China during the late Quaternary. Quat. Int. 503, 10–23.

Jia, Feifei, Lu, Ruijie, Gao, Shangyu, Li, Jinfeng, Liu, Xiaokang, 2015. Holocene aeolian activities in the southeastern Mu Us Desert, China. Aeolian Res. 19, 267–274.

Jiang, D., Tian, Z., 2013. East Asian monsoon change for the 21st century: results of CMIP3 and CMIP5 models. Chin. Sci. Bull. 58 (12), 1427–1435.

Kaboth-Bahr, S., Bahr, A., Zeeden, C., Yamoah, K.A., Lone, M.A., Chuang, C.-K., Löwemark, L., Wei, K.-Y., 2021. A tale of shifting relations: East Asian summer and winter monsoon variability during the Holocene. Sci. Rep. 11 (1), 6938.

Kidron, G.J., Yair, A., 2001. Runoff-induced sediment yield over dune slopes in the Negev Desert. 1: quantity and variability. Earth Surf. Process. Landforms J. Br. Geomorphol. Res. Group 26 (5), 461–474.

Krumbein, W.C., Pettijohn, F.J., 1938. Manual of Sedimentary Petrology. Appleton, Century, and Crofts, New York, p. 549.

Lancaster, N., 2020. On the formation of desert loess. Quat. Res. 96, 105–122.

Lancaster, N., Wolfe, S., Thomas, D., Bristow, C., Bubenzer, O., Burrough, S., Duller, G., Halfen, A., Hesse, P., Roskin, J., Singhvi, A., Tsoar, H., Tripaldi, A., Yang, X., Zárate, M., 2016. The INQUA Dunes Atlas chronologic database. Quat. Int. 410, 3–10.

Li, Xiang, 2020. The Research on Holocene Climate changes and Geomorphic evolution in the Mu Us desert, China. Thesis for Master's degree. Shanxi University.

Li, Baosheng, Zhang, David Dian, Jin, Heling, Wu, Zheng, Yan, Mancun, Sun, Wu, Zhu, Yizhi, Sun, Donghuai, 2000. Paleo-monsoon activities of Mu Us Desert, China since 150 ka B.P. — a study of the stratigraphic sequences of the Milanggouwan

Section, Salawusu River area. Palaeogeogr. Palaeoclimatol. Palaeoecol. 162 (1–2), 1–16. https://doi.org/10.1016/S0031-0182(00)00101-2.

Li, Baosheng, Wen, Xiaohao, Qiu, Shifan, Zhang, David Dian, Du, Shuhuan, Chen, Deniu, Ou, Xianjiao, Niu, Dongfeng, 2007. Phases of environmental evolution indicated by primary chemical elements and paleontological records in the Upper Pleistocene-Holocene Series for the Salawusu River Valley, China. Acta Geol. Sin. Engl. Ed. 81, 555–565.

Li, Shenghua, Sun, Jimin, Li, Bo, 2012. Holocene environmental changes in the central Inner Mongolia revealed by luminescence dating of the sediments from the Sala Us River valley. The Holocene 22 (4), 397–404.

Licent, E., De Chardin, Teilhard, Black, Davidson, 1926. On a presumably pleistocene human tooth from the Sjara-osso-gol(south-eastern Ordos) deposits. Bull. Geol. Soc. China 5 (3–4), 285–290.

Liu, Miaomiao, 2018. Aeolian Activity and Climatic Changes in the Mu Us Sandy Since the Last Glacial Maximum. Thesis for Master's degree. Shanxi University.

Liu, Kai, Lai, Zhongping, 2012. Chronology of Holocene sediments from the archaeological Salawusu site in the Mu Us desert in China and its palaeoenvironmental implications. J. Asian Earth Sci. 45, 247–255.

Liu, W., Yang, H., Sun, Y., Wang, X., 2011. δ13C Values of loess total carbonate: a sensitive proxy for Asian summer monsoon in arid northwestern margin of the Chinese loess plateau. Chem. Geol. 284 (3), 317–322.

Liu, Bing, Jin, Heling, Sun, Liangying, Sun, Zhong, Niu, Qinghe, Xie, Shengbo, Li, Guanhua, 2014a. Holocene moisture change revealed by the Rb/Sr ratio of aeolian deposits in the southeastern Mu Us Desert, China. Aeolian Res. 13, 109–119.

Liu, Z.Y., Wen, X.Y., Brady, E.C., Otto-Bliesner, B., Yu, G., Lu, H.Y., Cheng, H., Wang, Y.J., Zheng, W.P., Ding, Y.H., Edwards, R.L., Cheng, J., Liu, W., Yang, H., 2014b. Chinese cave records and the East Asia Summer Monsoon. Quat. Sci. Rev. 83, 115–128.

Liu, J., Chen, J., Zhang, X., Li, Y., Rao, Z., Chen, F., 2015. Holocene East Asian summer monsoon records in northern China and their inconsistency with Chinese stalagmite δ18O records. Earth Sci. Rev. 148, 194–208.

Liu, X., Lu, R., Du, J., Lyu, Z., Wang, L., Gao, S., Wu, Y., 2018. Evolution of peatlands in the Mu Us Desert, northern China, since the last deglaciation. J. Geophys. Res. Earth Surf. 123, 252–261. https://doi.org/10.1002/2017JF004413.

Liu, Xiaokang, Lu, Ruijie, Jia, Feifei, Chen, Lu, Li, Tengfei, Ma, Yuzhen, Wu, Yongqiu, 2018a. Holocene water-level changes inferred from a section of fluvio-lacustrine sediments in the southeastern Mu Us Desert, China. Quat. Int. 469, 58–67.

Lu, H.Y., Miao, X.D., Zhou, Y.L., Mason, J., Swinehart, J., Zhang, J.F., Zhou, L.P., Yi, S.W., 2005. Late Quaternary aeolian activity in the Mu Us and Otindag dune fields (north China) and lagged response to insolation forcing. Geophys. Res. Lett. 32 (21).

Lu, Yingxia, Li, Baosheng, Qiu, Shifan, Wang, Fengnian, Wen, Xiaohao, Niu, Dongfeng, Li, Zhiwen, 2010. Millennial-centennial scales climate changes of holocene indicated by magnetic susceptibility of high-resolution section in Salawusu River Valley, China. Chin. Geogr. Sci. 20 (3), 243–254.

Lu, H., Zhou, Y., Liu, W., Mason, J., 2012. Organic stable carbon isotopic composition reveals late Quaternary vegetation changes in the dune fields of northern China. Quat. Res. 77 (3), 433–444.

Lu, H., Wang, X., Wang, Y., Zhang, X., Yi, S., Wang, X., Stevens, T., Kurbanov, R., Marković, S.B., 2022. Chinese loess and the Asian monsoon: what we know and what remains unknown. Quat. Int. 620, 85–97.

Mason, Joseph A., Swinehart, James B., Huayu, Lu, Xiaodong, Miao, Phueng, Cha, Yali, Zhou, 2008. Limited change in dune mobility in response to a large decrease in wind power in semi-arid northern China since the 1970s. Geomorphology 102 (3–4), 351–363.

Mason, J.A., Lu, H., Zhou, Y., Miao, X., Swinehart, J.B., Liu, Z., Goble, R.J., Yi, S., 2009. Dune mobility and aridity at the desert margin of northern China at a time of peak monsoon strength. Geology 37, 947–950.

Niu, D., Li, B., Du, S., Wen, X., Qiu, S., Ou, X., Yang, Y.I., 2008. Cold events of Holocene indicated by primary elements distribution of the high-resolution sand dunes in the Salawusu River valley. J. Geogr. Sci. 18 (1), 01–16.

Pang, Yingjun, Wu, Bo, Jia, Xiaohong, Shi, Lin, Gaodabuxilatu, Li, Shizhong, 2019. Characteristics of wind regime and drift potential in Mu Us Sandy Land. J. Desert Res. 39 (1), 62–67 (in Chinese with an English abstract).

Parker, A.G., Eckersley, L., Smith, M.M., Goudie, A.S., Stokes, S., Ward, S., White, K., Hodson, M.J., 2004. Holocene vegetation dynamics in the northeastern Rub' al-Khali desert, Arabian Peninsula: a phytolith, pollen and carbon isotope study. J. Quat. Sci. 19 (7), 665–676.

Reimer, P.J., Baillie, M.G.L., Bard, E., Bayliss, A., Beck, J.W., Bertrand, C.J.H., Blackwell, P.G., Buck, C.E., Burr, G.S., Cutler, K.B., Damon, P.E., Edwards, R.L., Fairbanks, R.G., Friedrich, M., Guilderson, T.P., Hogg, A.G., Hughen, K.A., Kromer, B., McCormac, G., Manning, S., Ramsey, C.B., Reimer, R.W., Remmele, S., Southon, J.R., Stuiver, M., Talamo, S., Taylor, F.W., van der Plicht, J., Weyhenmeyer, C.E., 2004. IntCal04 terrestrial radiocarbon age calibration, 0–26 cal ka BP. Radiocarbon 46 (3), 1029–1058.

Reimer, P.J., Bard, E., Bayliss, A., Beck, J.W., Blackwell, P.G., Ramsey, C.B., Buck, C.E., Cheng, H., Edwards, R.L., Friedrich, M., Grootes, P.M., Guilderson, T.P., Haflidason, H., Hajdas, I., Hatte, C., Heaton, T.J., Hoffmann, D.L., Hogg, A.G., Hughen, K.A., Kaiser, K.F., Kromer, B., Manning, S.W., Niu, M., Reimer, R.W., Richards, D.A., Scott, E.M., Southon, J.R., Staff, R.A, Turney, C.S.M., van der Plicht, J., 2013. Intcal13 and Marine13 radiocarbon age calibration curves 0–50,000 years cal BP. Radiocarbon 55 (4), 1869–1887.

Shi, Yafeng, Zhaozheng, Kong, Sumin, Wang, Lingyu, Tang, Fubao, Wang, Tandong, Yao, Xitao, Zhao, Peiyuan, Zhang, Shaohua, Shi, 1993. Mid-Holocene climates and environments in China. Glob. Planet. Change 7 (1–3), 219–233.

Shi, P., Lu, H., Leung, L.R., He, Y., Wang, B., Yang, K., Yu, L., Liu, L., Huang, W., Xu, S., Liu, J., Huang, X., Li, L., Lin, Y., 2021. Significant land contributions to interannual predictability of East Asian Summer Monsoon Rainfall'. Earth's Future 9 (2) e2020EF001762.

Shu, Peixian, Baosheng, Li, Dongfeng, Niu, et al., 2016. Climate Variations Recorded by the Grain-size from the DGS1 Segment in the Southeast of China's Mu Us Desert during the Holocene. Sci. Geogr. Sin. 36 (3), 448–457 (Chinese with an English abstract).

Smith, B.J., Wright, J.S., Whalley, W.B., 2002. Sources of non-glacial, loess-size quartz silt and the origins of "desert loess". Earth Sci. Rev. 59 (1), 1–26.

Steinke, S., Glatz, C., Mohtadi, M., Groeneveld, J., Li, Q., Jian, Z., 2011. Past dynamics of the East Asian monsoon: no inverse behaviour between the summer and winter monsoon during the Holocene. Glob. Planet. Chang. 78 (3), 170–177.

Stuiver, M., Reimer, P.J., Bard, E., Beck, J.W., Burr, G.S., Hughen, K.A., Kromer, B., McCormac, G., Vander, Plicht J., Spurk, M., 1998. INTCAL98: Radiocarbon age calibration, 24,000–0calBP. Radiocarbon 40, 1041–1083.

Sun, Jimin, 2000. Origin of eolian sand mobilization during the past 2300 years in the Mu Us Desert, China. Quat. Res. 53, 73–88.

Sun, J.M., 2002. Provenance of loess material and formation of loess deposits on the Chinese Loess Plateau. Earth Planet. Sci. Lett. 203 (3–4), 845–859.

Sun, Q., Wang, H.J., 2012. Changes of the connection between the summer North Atlantic Oscillation and the East Asian summer rainfall. J. Geophys. Res.-Atmos. 117.

Sun, J., Yin, G., Ding, Z., Liu, T., Chen, J., 1998. Thermoluminescence chronology of sand profiles in the Mu Us Desert, China. Palaeogeogr. Palaeoclimatol. Palaeoecol. 144 (1), 225–233.

Telfer, M.W., Hesse, P.P., 2013. Palaeoenvironmental reconstructions from linear dunefields: recent progress, current challenges and future directions. Quat. Sci. Rev. 78 (0), 1–21.

Wang, Luo, Li, Jingjing, Lu, Houyuan, Gu, Zhaoyan, Rioual, Patrick, Hao, Qingzhen, Mackay, Anson, Jiang, Wenying, Cai, Binggui, Xu, Bing, Han, Jingtai, Chu, Guoqiang, 2012. The East Asian winter monsoon over the last 15,000 years: its links to high-latitudes and tropical climate systems and complex correlation to the summer monsoon. Quat. Sci. Rev. 32, 131–142.

Wang, Haipeng, Chen, Jianhui, Zhang, Xiaojian, Chen, Fahu, 2014. Palaeosol development in the Chinese Loess Plateau as an indicator of the strength of the East Asian summer monsoon: evidence for a mid-Holocene maximum. Quat. Int. 334-335, 155–164.

Wang, Fengnian, Si, Yuejun, Li, Baosheng, Niu, Dongfeng, Li, Zhiwen, Wen, Xiaohao, Yang, Zhiying, 2021. Variations in the aeolian sequence Zr/Rb ratios in the Mu Us Desert during the Holocene and their implications for the East Asian monsoon. Aeolian Res. https://doi.org/10.1016/j.aeolia.2021.100753.

Wen, Xiaohao, Li, Baosheng, Zheng, Yanming, Zhang, David Dian, Ye, Jianping, 2009. Climate variability in the Salawusu River valley of the Ordos Plateau (Inner Mongolia, China) during Marine Isotope Stage 3. J. Quat. Sci. 24 (1), 61–74.

Wen, Y., Wu, Y., Tan, L., Li, D., Fu, T., 2019. End-member modeling of the grain size record of loess in the Mu Us Desert and implications for dust sources. Quat. Int. 532, 87–97.

Wen, Penghui, Wang, Nai'ang, Wang, Yixin, Huang, Yinzhou, Cheng, Hongyi, He, Tonghui, 2021. Fluvial incision caused irreversible environmental degradation of an ancient city in the Mu Us Desert, China. Quat. Res. 99, 1–13.

Williams, A.N., 2012. The use of summed radiocarbon probability distributions in archaeology: a review of methods. J. Archaeol. Sci. 39 (3), 578–589.

Wu, Yongsheng, Hasi, Eerdun, Wugetemole, Wu, Xia, 2012. Characteristics of surface runoff in a sandy area in southern Mu Us sandy land. Chin. Sci. Bull. 57 (2–3), 270–275. https://doi.org/10.1007/s11434-011-4728-0.

Xia, D., Jia, J., Li, G., Zhao, S., Wei, H., Chen, F., 2014. Out-of-phase evolution between summer and winter East Asian monsoons during the Holocene as recorded by Chinese loess deposits. Quat. Res. 81 (3), 500–507.

Xiao, Jule, Xu, Qinghai, Nakamura, Toshio, Yang, Xiaolan, Liang, Wendong, Inouchi, Yoshio, 2004. Holocene vegetation variation in the Daihai Lake region of north-central China: a direct indication of the Asian monsoon climatic history. Quat. Sci. Rev. 23, 1669–1679.

Xu, Z.W., Mason, J.A., Xu, C., Yi, S.W., Bathiany, S., Yizhaq, H., Zhou, Y.L., Cheng, J., Holmgren, M., Lu, H.Y., 2020. Critical transitions in Chinese dunes during the past 12,000 years. Sci. Adv. 6 (9), 10.

Yang, Xiaoping, Liang, Peng, Zhang, Deguo, Li, Hongwei, Rioial, Patrick, Wang, Xulong, Xu, Bing, Ma, Zhibang, Liu, Qianqian, Ren, Xiaozong, Hu, Fangen, He, Yuxin, Rao, Gang, Chen, Ninghua, 2019. Holocene aeolian stratigraphic sequences in the eastern portion of the desert belt (sand seas and sandy lands) in northern China and their palaeoenvironmental implications. Sci. China Earth Sci. 62 (8), 1302–1315.

Yuan, Baoyin, 1978. Sedimentary environment and stratigraphic subdivision of the Sjara Osso-Gol Formation. Sci. Geol. Sin. 3, 220–234 (In Chinese with English abstract).

Zhang, Xinshi, 1994. Principles and optimal models for development of Maowusu sandy grassland. Acta Phytoecol. Sinica 18 (1), 1–16.

Zhang, Y., Zhu, K., Huang, C., Kong, D., He, Y., Wang, H., Liu, W., Xie, Z., Wei, G., Liu, Z., 2019. Asian Winter Monsoon Imprint on Holocene SST changes at the Northern Coast of the South China Sea. Geophys. Res. Lett. 46 (22), 13363–13370.

Zhang, H., Zhang, X., Cai, Y., Sinha, A., Spötl, C., Baker, J., Kathayat, G., Liu, Z., Tian, Y., Lu, J., Wang, Z., Zhao, J., Jia, X., Du, W., Ning, Y., An, Z., Edwards, R.L., Cheng, H., 2021. A data-model comparison pinpoints Holocene spatiotemporal pattern of East Asian summer monsoon. Quat. Sci. Rev. 261, 106911.

Zhao, Y., Yu, Z., Chen, F., 2009. Spatial and temporal patterns of Holocene vegetation and climate changes in arid and semi-arid China. Quat. Int. 194 (1), 6–18.

Zhao, Hui, Sheng, Yongwei, Li, Bo, Fan, Yuxin, 2016. Holocene environment changes around the Sara Us River, northern China, revealed by optical dating of lacustrine-aeolian sediments. J. Asian Earth Sci. 120, 184–191. https://doi.org/10.1016/j.jseaes.2016.02.002.

Zhou, W., Chui, Y., Yang, L., Cheng, P., Chen, N., Ming, G., Hu, Y., Li, W., Lu, X., 2022. 14C geochronology and radiocarbon reservoir effect of reviewed lakes study in China. Radiocarbon 64 (4), 833–844.